Nonlinear pattern formation near the onset of Rayleigh-Bénard convection

H. S. Greenside* and W. M. Coughran, Jr.
AT&T Bell Laboratories, Murray Hill, New Jersey 07974
(Received 15 September 1983)

A two-dimensional relaxational model equation is studied numerically to investigate the role of lateral boundaries and nonlinear terms in pattern formation. The model reduces in perturbation theory to the same amplitude equation as the one derived from the three-dimensional Boussinesq equations for thermal convection. State-of-the-art numerical methods are described that solve the initial-boundary-value problem efficiently and accurately in large rectangular cells and for long times, for both rigid and periodic boundary conditions. The results of simulations for different aspect ratios, Rayleigh numbers, and initial conditions are discussed in detail. The interaction of defects, the effect of lateral boundaries on the growth and saturation of linear instabilities, and the origin of the long-time scales needed to reach a stationary state are studied. Wave-number selection is investigated using spatial Fourier analysis, and evidence is presented that the band of stable wave numbers is not uniformly occupied as a pattern evolves from random initial conditions of all length scales. These results are in good agreement with many of the observed experimental features of pattern formation in small- and large-aspect-ratio cells, and show some new features that have not yet been seen.

I. INTRODUCTION

The nature of turbulence, the way in which a driven dissipative system evolves in time and in which scalar and vector quantities are transported during this evolution, has yet to receive a satisfactory theoretical or experimental explanation. The main difficulties are the stochastic time dependence and the many orders of spatial and temporal scales often involved. In the last fifteen years, the difficult question "what is turbulence" has been approached from a different and fruitful point of view, namely, how does turbulence commence? More precisely, scientists have been exploring analogies between the transition to turbulence and second-order phase transitions of condensed-matter systems, the latter now having attained a quantitative and mature level of understanding.[1] When a nonequilibrium system evolves to a stationary state, a further analogy has been pursued, namely, to what extent the spatial degrees of freedom constitute a broken symmetry similar to that found in equilibrium systems such as crystals, magnets, or superfluids.[2] This is the question of pattern formation: How does a stationary nonequilibrium system distribute energy and momentum among its stable modes, what length scales are determined, and how are possible spatial degeneracies resolved?

To answer these questions, considerable theoretical and experimental effort has been devoted to one of the simplest nonequilibrium systems: Rayleigh-Bénard convection[3,4,5] (see Fig. 1). This system is simple because the boundary conditions are static and homogeneous, because the fluid is contained in experimental cells that can be precisely engineered and accurately controlled, and because the complexity of the fluid motion increases slowly as the fluid is driven further from equilibrium. For a critical temperature gradient between the upper and lower plates (equivalently at a critical Rayleigh number R_c), buoyancy forces overcome the dissipative effects of viscous shear and thermal conduction, and the motionless fluid spontaneously breaks up into convective cells or rolls of upward- and downward-moving regions of fluid. The various analogies with phase transitions and broken symmetries have been carefully investigated just above this transition point from conduction to convection.[6,7,8]

It is a surprising and disturbing fact that even just above the onset of convection, when only a few length and time scales are involved, the physics of the fluid motion is not fully understood. For small-aspect-ratio cells ($\Gamma \lesssim 5$), the fluid becomes stationary after about a horizontal diffusion time, τ_h, and convective rolls appear with a wavelength comparable to the depth of the fluid, usually perpendicular to the lateral boundaries.[9,10,11] In this regime,

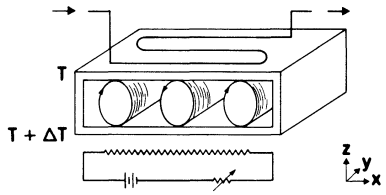

FIG. 1. Geometry of a Rayleigh-Bénard cell (the front and back walls are not shown). The convecting fluid lies between two horizontal perfectly conducting plates. A variable heat source below and a heat sink above (e.g., water flowing through pipes) generate a vertical temperature gradient in the same direction as gravity. Fluid and cell are characterized by three dimensionless parameters: the Rayleigh number $R=\alpha g\,\Delta T\,d^3/\nu\kappa$, the Prandtl number $\sigma=\nu/\kappa$, and the aspect ratio $\Gamma=L/d$. Here α is the coefficient of thermal expansion for the fluid, g is the gravitational acceleration, ΔT is the temperature difference between the horizontal plates, d is the depth of the fluid, ν is the kinematic viscosity, κ is the thermal diffusivity, and L is a characteristic horizontal dimension.

the physics is partly understood because the temporal behavior often resembles that observed in simple low-dimensional dynamical systems, such as sets of ordinary differential equations or discrete recursion maps.[12] For increasing Rayleigh numbers, the fluid undergoes sharp symmetry-breaking bifurcations[13] that follow one of a few possible scenarios. Although a given scenario cannot yet be predicted in advance, some scenarios have been shown to have universal characteristics similar to those found in critical phenomena.[14,15]

For large aspects ratios ($\Gamma \gtrsim 20$), the experimental data are ambiguous and conflicting. One experiment in a large cylindrical cell ($\Gamma \sim 60$) using liquid helium for the convecting fluid (which had a Prandtl number of $\sigma \simeq 3$) showed turbulence, i.e., a nonperiodic time dependence, as soon as the fluid started convecting.[16,17] This cryogenic experiment used a constant heat current instead of a constant temperature gradient to obtain higher precision and measured the time dependence of the Rayleigh number (which can then be related to the vertical heat transport or Nusselt number[18]). The difficulty of suspending particles in the liquid helium prevented identification of the spatial flow corresponding to the observed turbulence. More recent optical experiments in large rectangular cells, with water ($\sigma \gtrsim 2.5$) as the convecting fluid, show a clear time dependence a finite distance in Rayleigh number above onset.[19] This coincides roughly with the onset of a secondary instability, the skewed-varicose instability first analyzed by Busse and Clever.[20] Closer to onset, over periods lasting as long as a hundred horizontal diffusion times, these room-temperature experiments sometimes reach a stationary state.[19] These different conclusions about the presence of turbulence just above the onset of convection may be due to the different geometries of the container, to the different thermal boundary conditions, to the different aspect ratios (the largest rectangular cell studied was half as large as the largest cylindrical cell) or to a combination of these effects. The optical experiments suggest that the pattern formation is always influenced by the lateral boundaries (convection rolls evolve to become normal to these boundaries) and dominated by the motion and interaction of defects or irregularities in convection rolls.

In this paper, we theoretically investigate pattern formation near the onset of Rayleigh-Bénard convection in small- and large-aspect-ratio rectangular cells. While the motion of a single defect or pair of defects in a laterally infinite cell is partially known analytically,[21,22] the motion of many defects, or of a defect in a finite cell, is already too difficult for analytical solution. We therefore study the problem numerically with the goal of identifying the essential mechanisms of pattern formation and relating these calculations both to experiment and to some of the issues previously discussed about equilibrium systems.

The two-dimensional model equation we study reduces in perturbation theory to the amplitude equation derived from the three-dimensional Boussinesq equations by Newell and Whitehead[23] and Segel.[24] For sufficiently large aspect ratios and sufficiently close to onset, this model will have the same long-wavelength, long-time behavior as the fluid and heat equations. One important conclusion of our paper is that the model also seems to describe the shorter-length scales accurately, e.g., the interaction of defects or the motion of defects in the presence of lateral boundaries. Since the model is purely relaxational, we cannot explain the existence of turbulence near onset. Indeed, for this equation the mean square of the field, which is equivalent to the heat transport or Nusselt number, increases monotonically during the long transient leading to a stationary state. This is inconsistent with the clearly nonperiodic time dependence seen in the cryogenic experiment.[16] It is unlikely that this experiment can be explained by a transient lasting longer than the observation time (which was $25\tau_h$). Some other physical mechanism is needed that makes the evolution nonrelaxational.

There are several related theoretical issues that we also investigate in their own right. One is the effect of lateral boundaries *and* nonlinearities on pattern formation. The eigenfunctions of our linearized model in a large domain are highly degenerate[25] and suggest a greater complexity of fluid motion than that observed experimentally.[9,19] Our results suggest that, close to onset, only a few patterns are realized starting from random initial conditions and that the degeneracy of the nonlinear stationary states is small. An equivalent observation is that, sufficiently close to onset, the barriers for defect motion are small and arbitrarily complicated configurations of defects will succeed in evolving to one of the few stationary states.

Another issue is the way that various linear instabilities grow and saturate, especially in the presence of boundaries. Various papers by Busse and collaborators[4,20,76,81] show how invaluable a linear stability analysis can be for understanding the time dependence, wave-number selection, and evolution of convection experiments in a finite container. This is so even though they studied the linear stability of straight parallel rolls in an infinite cell. Because of the difficulties of solving the three-dimensional initial-boundary-value problem given by the Boussinesq equations, there are still some questions about how instabilities, such as the zigzag, cross-roll, and Eckhaus instabilities are affected by boundaries and what they grow into. We give a preliminary answer by solving the initial-boundary-value problem for our model (which has many of the same instabilities). We find that most instabilities are quenched near the lateral walls and that defects are created as some of the instabilities grow.

A further issue is the time scale needed for the relaxational model to reach a stationary state. For a given geometry, the natural time scale expected for the flow to become stationary is a horizontal-thermal-diffusion diffusion time;[19] i.e., the time for a thermal perturbation to diffuse across a characteristic horizontal dimension of the cell. Experiments suggest that the time scale for large-aspect-ratio cells to become stationary is often much larger than a horizontal-diffusion time;[19] the time scale is not obviously related to the dimensions of the cell. By studying pattern evolution in large-aspect-ratio cells with *periodic* boundary conditions, we show that the long-time scale *does not* arise from the complexity of the dynamics of interacting defects (as we suggested previously[26]) but instead is a consequence of the presence of rigid boun-

daries and two length scales,[8] leading to a competition between boundary and bulk effects. Our calculations also suggest that the long-time scale does not derive from rare noise-induced transitions over barriers from one stationary state to another.

A final theoretical issue we study is wave-number selection in stationary states. Because the transition to convection is continuous and occurs at a finite wave number, only a finite band of wave numbers can be stable near onset. Starting from random initial conditions of all length scales, the question then arises whether all stable wave numbers are found in the final stationary state. Experiments suggest this is not the case,[27–29] and several ingenious attempts have been made to deduce a nonlinear wave-number selection principle to explain these results.[30–35] One difficulty, especially in a bounded cell with a finite density of defects, is how to define what is meant by a wave number. A possibility recently suggested by Gollub and McCarriar[28] is to spatially Fourier analyze some fluid field and compare the resulting power spectrum with the range of stable wave numbers determined by a stability analysis. We have adopted this approach and have studied wave-number selection in our model. For typical experimental aspect ratios, the resolution in spectral width arising from the finite lateral dimensions is larger than the stability band near onset for our model and no conclusions can be made. However, for larger Rayleigh numbers (in a regime for which our model is no longer hydrodynamically correct) our calculations indicate that only a small part of the stable band is finally occupied, centered around the critical wave number.

The model we study has already been discussed by several authors who were concerned primarily with wave-number selection in one-dimensional geometries for which the analysis is easier.[32–35] The work most closely related is a recent paper by Cross[8] who qualitatively analyzed the possible stationary states for different geometries close to onset. For example, Cross explained why rolls evolve normal to boundaries, why concentric rings of rolls are *not* necessarily found in cylindrical containers, and when defects are to be expected. Our work closely complements that of Cross in investigating the *dynamics* of the model, how stationary states are achieved, and by giving specific examples of stationary patterns. The present work together with that of Cross[8] shows that three-dimensional dynamics on short length and time scales can also be studied with two-dimensional model equations.

The paper is organized as follows. In Sec. II we discuss the model equation, its relation to the three-dimensional Boussinesq equations, and some of its features that can be deduced analytically. In Sec. III we discuss how the model is solved numerically. In Sec. IV we present the results of numerous simulations in small and large cells and study defect motion. In Sec. V we use periodic boundary conditions to study pattern formation and defect motion in the absence of rigid walls and corners. In Sec. VI we discuss the growth and saturation of linear instabilities in the presence of boundaries, and in Sec. VII the results of using spatial Fourier analysis to study wave-number selection are presented. Finally in Sec. VIII we summarize the previous sections and suggest some new directions that would be useful to investigate. Some of the conclusions presented here have already appeared in two shorter publications.[26,36]

II. A TWO-DIMENSIONAL MODEL OF THREE-DIMENSIONAL CONVECTION

Close to the onset of convection, experiment shows that the fluid motion consists of locally parallel convection rolls near the critical wave number. The orientation and mean velocity of the rolls change slowly over several roll diameters and over many vertical diffusion times.[19] This suggests that the equations of motion can be simplified and restated in terms of a complex envelope or amplitude function that depends on "slow" variables (scaled variables that change slowly compared to the original "fast" space and time coordinates as one approaches a bifurcation). The magnitude and phase of this envelope slowly modulate the locally sinusoidal motion of the temperature, pressure, and velocity fields.

Using a singular-multiscale-perturbation theory to separate the slow and fast temporal and spatial scales, Newell and Whitehead[23] and Segel[24] succeeded in deriving such an amplitude equation in the slow variables as the lowest-order nontrivial solubility condition to be satisfied in the expansion of the Boussinesq equations. The expansion parameter was the reduced Rayleigh number,

$$\epsilon = R/R_c - 1$$

(R_c is the critical Rayleigh number for a laterally infinite cell), which measures the distance above onset. Using the amplitude equation, one could concisely study the linear stability of parallel or superimposed rolls and the way that inhomogeneities in the amplitude or phase propagate.[23] Since the equation was derived on the assumption that the coordinates were aligned along locally parallel rolls, it could not be used to study defects or other irregularities in the roll structure that vary too rapidly in space as near the corner of a rectangular cell. It is currently not known how to generalize the Newell-Whitehead-Segel equation to describe such features using only slow variables.

Because the amplitude equation was simple and involved only horizontal space coordinates, it turned out to be easy to guess a two-dimensional rotationally invariant equation in fast variables that reduced in a similar singular-perturbation expansion to the *same* amplitude equation. The two-dimensional equation therefore would have the same linear instabilities and diffusive properties on slow scales as the Boussinesq equations. This equation, first derived by Swift and Hohenberg in another context,[7] was

$$\tau_0 \partial_t \phi = [\epsilon - (\xi_0^2/4k_0^2)(\Delta + k_c^2)^2]\phi - g\phi^3 ,$$

where τ_0 and ξ_0 are characteristic time and length scales of order 1 and can be derived, as can g, from the expansion of the Boussinesq equations depending on what boundary conditions are assumed;[37,38] k_c is the critical wave number minimizing R_c. The real field $\phi(x,y,t)$ can be considered an original (unscaled) fluid field in a given horizontal plane, e.g., the vertical velocity component in the midplane of the convection cell. It can also be considered

an order parameter that is zero in the conducting state ($\epsilon \leq 0$) and nonzero otherwise. By rescaling the field and coordinates and by setting $k_c = 1$ (so a roll diameter is now π) we arrive at the model equation

$$\partial_\tau \phi = [\epsilon - (\Delta + 1)^2]\phi - \phi^3 , \tag{1}$$

where the scaled variable τ is in units of the vertical diffusion time. This nonlinear biharmonic equation should approximate the slow scale behavior of the Boussinesq equations in the limit of vanishing ϵ.

Using hindsight, this equation could have been derived without reference to the Boussinesq equations and the amplitude equation. The continuous onset at a finite wavelength requires the eigenvalue, λ, of a mode of wave number k to have the quadratic dependence

$$\lambda = \epsilon - (1-k)^2 . \tag{2}$$

For small ϵ and λ just positive, $k \simeq 1$ and we can write

$$(1-k)^2 \cong \tfrac{1}{4}(1+k)^2(1-k)^2 = \tfrac{1}{4}(1-k^2)^2 .$$

This suggests (after rescaling) the linear operator $\epsilon - (1+\Delta)^2$. The cubic nonlinearity follows from the basic symmetry of the fluid fields on reflection through the midplane of the convection cell; non-Boussinesq effects such as a temperature-dependent viscosity or an asymmetric thermal profile will lead to quadratic terms as well.[39] Thus Eq. (1) is general and has, in fact, appeared in several different contexts such as convection,[40,41] chemical reaction-diffusion systems,[42] and flame propagation.[43]

Since Eq. (1) is fourth order in its spatial derivatives, two independent constraints must be imposed on the field at the boundaries to give a well-posed initial-boundary-value problem. For the case of "rigid" boundary conditions, we follow Cross[8,44] and require

$$\phi = \partial_n \phi = 0 \tag{3a}$$

on all lateral walls, where ∂_n is the normal derivative. To lowest order in the expansion parameter ϵ, Eq. (3a) reproduces the rigid boundary conditions on the complex amplitude function of the Boussinesq equations when ϕ is expressed in terms of the latter.[8] For periodic boundary conditions, we require continuity of ϕ and its normal derivatives across opposite sides

$$\begin{aligned} &\phi(0,y) = \phi(L_x,y) , \quad \partial_n \phi(0,y) = \partial_n \phi(L_x,y) , \\ &\phi(x,0) = \phi(x,L_y) , \quad \partial_n \phi(x,0) = \partial_n \phi(x,L_y) \end{aligned} \tag{3b}$$

for $0 \leq x \leq L_x$ and $0 \leq y \leq L_y$. Equation (1) with the boundary conditions of Eq. (3a) or (3b) are the model we solve to investigate the influence of lateral walls on pattern formation. To understand when this model can be related to experimental data and what properties have been analytically derived, several important physical points should be made.

First, Eq. (1) is purely dissipative, unlike the Boussinesq equations to which it is related. This follows from the existence of the Lyapunov functional

$$F[\phi] = \int dx\, dy \{ -\epsilon\phi^2 + \tfrac{1}{2}\phi^4 + [(\Delta+1)\phi]^2 \} , \tag{4}$$

from which Eq. (1) can be variationally derived and which decreases monotonically for all initial conditions.[8] The latter property proves that Eq. (1) must always relax to a stationary state and cannot have a periodic or nonperiodic time dependence. The existence of the Lyapunov functional, Eq. (4), depends on the particular functional form of the nonlinearity in Eq. (1). Rotationally invariant terms such as $\phi^2 \Delta\phi$ and $\phi(\vec{\nabla}\phi)^2$ cannot be derived variationally and the corresponding equations would no longer be rigorously relaxational. However, numerical tests show that nonpotential evolution with these terms near onset is similar to the potential flow of Eq. (1) near onset and for large cells (see Sec. III).

As Cross has shown,[8] stationary solutions of Eqs. (1) and (3) can be ordered by comparing their associated values of the Lyapunov functional F. Because Eq. (4) decreases monotonically for all initial conditions, a stationary solution can transform, in the presence of noise and over a long enough time, to a state that has a lower Lyapunov value. For a given cell geometry and reduced Rayleigh number, Eq. (4) can thus be used to determine those stationary states a given state can transform into and perhaps suggest the most stable state, which has the lowest value. It should be kept in mind that a lower value of F does not necessarily imply greater stability. The relative stability of two states with respect to fluctuations depends on the heights of various barriers linking the states and not on their values of F (see Fig. 2).

A second physical point is that the Prandtl number σ, which measures the relative strength of the viscous and conduction modes of dissipation in the Boussinesq equations, does not enter Eq. (1) independently but only through the definition of the scaled variables or through terms of higher order in ϵ. [Similarly details of the lateral thermal boundary conditions enter only at higher order[34] in Eq. (3)]. In tracing the derivation of the amplitude equation for stress-free horizontal boundaries, one finds that the nonlinear term comes solely from the heat equa-

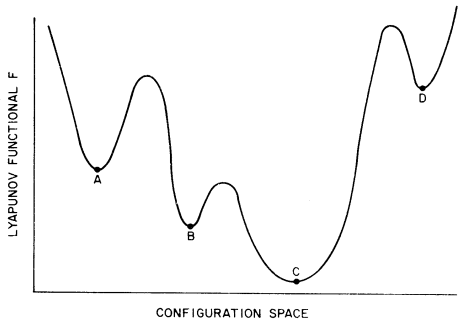

FIG. 2. One-dimensional schematic plot of the dependence of the Lyapunov functional, Eq. (4), on the configuration space of solutions to Eq. (1). Initial conditions start somewhere on this curve and evolve downhill until an extremum, corresponding to a stationary state, is reached. In the presence of noise and over long times, a stationary solution can transform to a state of lower Lyapunov value (Ref. 8). Lower states are not necessarily more stable than higher states; e.g., the barriers surrounding state A are larger than those of states B and D, and A is more stable with respect to fluctuations. State C is the lowest and most stable state.

tion. It is unchanged if the nonlinear term in the Navier-Stokes equations is dropped, corresponding to the limit of infinite Prandtl number.[23] Thus the solutions of Eq. (1) are best compared with large Prandtl number fluids. For small Prandtl numbers, higher-order terms in the expansion giving the amplitude equation, which relate the curvature of the rolls to the generation of vertical vorticity, become important.[45,46] These terms make the motion nonrelaxational and introduce new secondary instabilities such as the oscillatory and skewed-varicose instabilities.[45] For rigid boundary conditions, these terms are higher order in ϵ and can be ignored for sufficiently small ϵ and large σ (so that[45] $\epsilon/\sigma^2 \ll 1$ or for small ϵ when $\sigma=0$). Since Eq. (1) does not include the generation of vertical vorticity, the solutions will reveal to what extent motion can occur without this mechanism, whose importance has been emphasized by Whitehead[47] and discussed by Siggia and Zippelius.[21]

Equation (1) involves several approximations that prevent a quantitative comparison of its solutions with experiment. We have already mentioned that the boundary conditions, Eq. (3a), and the quadratic dependence of the eigenvalue on wavenumber Eq. (2), are correct only to lowest order in ϵ. The cubic nonlinearity in Eq. (1) is a real-space approximation to a cubic sum of Fourier modes of ϕ which, acting on the Fourier component, $\phi_{\vec{k}}$, has the following form:[38]

$$\sum_{\vec{k}_1,\vec{k}_2,\vec{k}_3} g(\vec{k},\vec{k}_1,\vec{k}_2,\vec{k}_3)\phi_{\vec{k}_1}\phi_{\vec{k}_2}\phi_{\vec{k}_3}\delta_{\vec{k}+\vec{k}_1,\vec{k}_2+\vec{k}_3} . \quad (5)$$

For superimposed rolls, we see that the real-space nonlinear term should be a nonlocal integral operator (convolution).[8] Since the coupling function g depends on the angles between superimposed rolls,[38] our simple cubic term with $g=1$ will have the wrong angle dependence for the cross-roll instability. This is a minor problem since the solutions of Eq. (1) rapidly evolve to have only locally parallel rolls nearly everywhere. A final approximation to mention is that the amplitude equation and Eq. (1) are derived by retaining only the fundamental mode in the vertical direction ($\sin\pi z$ for free-slip boundary conditions) and its first harmonic, i.e., the first two terms in a Galerkin expansion in the z variable. Equation (1) becomes incorrect when the thermal profile becomes nonlinear and develops thermal boundary layers[4] near the surfaces of the horizontal plates. This would require more modes to obtain adequate resolution in the vertical direction.

As we mentioned above, several features of Eq. (1) can be derived analytically[8,23] and are useful for interpreting the numerical simulations presented later. The field ϕ together with the normalized eigenfunctions of the linearized Boussinesq equations suffice to recover the temperature, pressure, and velocity fields to lowest order in ϵ.[8] With these expressions, one can then show that the dimensionless vertical heat transport is known to lowest order and is given by the following:

$$N=1+\frac{1}{1+\epsilon}\langle\phi^2\rangle , \quad (6)$$

where $\langle\ \rangle$ denotes an average over horizontal coordinates. For larger ϵ, Eq. (6) no longer physically corresponds to the Nusselt number but still provides a useful, global, phase-independent measure of the field ϕ. From the amplitude equation,[23] one can show that the amplitude, when it goes to zero near the boundaries or near a defect, heals to its average value far away over a length scale of size $\epsilon^{-1/2}$ or $\epsilon^{-1/4}$ (with a constant prefactor of order one that we ignore). Thus in the regime $1 \ll \epsilon^{-1/2} \ll \Gamma$, Eq. (1) will have boundary layers near the lateral wall and near "core" regions around isolated defects over which the convection is suppressed on a length scale $\epsilon^{-1/2}$. Also in this regime, the Lyapunov functional, Eq. (4), can be expressed as a sum of competing terms. These terms arise from a lateral-wall term that forces rolls to be normal to minimize the boundary layer over which convection is suppressed; from a bulk term that forces rolls far away from the lateral walls to be straight and parallel; and from a defect term that determines the extent to which convection is suppressed near the defect core. In the limit $\epsilon \to \epsilon_c$ (where ϵ_c is the smallest value for a finite cell that allows a stable nonzero solution), the bulk term dominates, defects are eliminated, and only parallel rolls occur. (This has been verified numerically using the methods described in the next section.) For $\epsilon > \epsilon_c$, a subtle balance occurs in which the rolls try to be everywhere normal to the walls and parallel in the interior of the cell.[8] Our simulations are carried out primarily in the regime $\epsilon^{-1/2} \ll \Gamma$ and will illustrate how this balance is achieved in a rectangular cell as a function of ϵ.

III. NUMERICAL SOLUTION OF THE MODEL EQUATION

Although Eq. (1) is an immense simplification of the Boussinesq equations, it is still not trivial to solve the initial-boundary-value problem for the long-time scales and large aspect ratios relevant to experiment. The crucial step is the observation that Eq. (1) can be solved by the repeated solution of the *linear* constant-coefficient biharmonic problem

$$(\Delta^2+a\Delta+b)u=f_1 , \quad (7a)$$

$$u\,|_{\partial R}=f_2$$

and (7b)

$$\partial_n u\,|_{\partial R}=f_3$$

on a rectangular domain R where a and b are real numbers, ∂R denotes the boundary of the domain, and f_1, f_2, and f_3 are given functions. Different kinds of boundary conditions then require different numerical algorithms for the efficient solution of Eq. (7). For the case of rigid boundaries, given by Eq. (3a) [equivalently $f_2=f_3=0$ in Eq. (7b)], we have used a recent algorithmic advance[48] which can solve Eq. (7) with an effort proportional to the number of mesh points covering R. (The method assumes a rectangular geometry. A similar method is possible but has not yet been implemented for circular domains.[49] Solutions of Eq. (1) have been calculated by a different method for a medium-aspect-ratio cylindrical cell by Manneville.[50]) For the case of periodic boundary condi-

tions on all sides, Eq. (3b), the solution of Eq. (7) is straightforward and is easily carried out by spectral methods.[51] In the following we concentrate on the case of rigid boundaries which is more relevant to experiment. We describe how the nonlinear problem is reduced to repeated solutions of the linear problem, Eq. (7), how the numerical errors are monitored and controlled, how the initial conditions are chosen, and finally we describe some useful data summarizing our experience with runs on a Cray Research Cray-1 computer.

To obtain good numerical integrating efficiency we used an *implicit* backward Euler time-integration scheme[52] with a variable-step size, variable-order time-step monitor.[53] [Because Eq. (1) has fourth-order spatial derivatives, numerical stability would require the time step of an explicit time-integration scheme to be bounded by the fourth power of the spatial mesh size, a severe restriction.] The backward Euler time discretization leads to a series of nonlinear static problems of the form

$$\frac{\phi(\tau+\Delta\tau)-\phi(\tau)}{\Delta\tau}=L\phi(\tau+\Delta\tau)-[\phi(\tau+\Delta\tau)]^3 , \tag{8}$$

where $\phi(\tau)$ is the known solution of Eqs. (1) and (3) at time τ, $\Delta\tau$ is the step size (discussed further below), $L=\epsilon-(1+\Delta)^2$ is a linear biharmonic operator, and $\phi(\tau+\Delta\tau)$ is the unknown implicit solution at the next time step that we are seeking. (We have temporarily suppressed spatial indices.) We solve the spatial problem, Eq. (8), by a multi-iteration approximate-Newton scheme in which the nonlinear problem is reduced to a linear one (outer iterations) and then another level of iteration is used to reduce the linear problem to the form Eq. (7) (inner iterations).

To solve Eq. (8), we assume that $\phi(\tau+\Delta\tau)$ is obtained by successive approximations of the form

$$\phi(\tau+\Delta\tau)\simeq\phi_{k+1}=\phi_k+\delta_k , \quad \phi_0=\phi(\tau) , \tag{9}$$

where $\phi_k(x,y)$ is the approximation at the kth iteration and the outer correction field $\delta_k(x,y)$ is assumed to be small [$||\delta_k|| \ll ||\phi_k||$ in the maximum norm $||f(x,y)|| = \max_{x,y} |f(x,y)|$]. Substituting Eq. (9) into Eq. (8) and linearizing in the small field δ_k gives us the Newton equations for the unknown corrections δ_k:

$$\left[L-\frac{1}{\Delta\tau}-3\phi_k^2\right]\delta_k=\phi_\tau(k)-(L\phi_k-\phi_k^3) , \tag{10}$$

where the time derivative is approximated by

$$\phi_\tau(k)=\frac{\phi_k-\phi_0}{\Delta\tau} . \tag{11}$$

The right-hand-side (rhs) field of Eq. (10) is the kth outer residual, $r_{\text{outer}}(k)$, and measures to what extent Eq. (8) is satisfied. Given the residual, we would like to invert Eq. (10) to get the outer correction, δ_k, and then get a better approximation to $\phi(\tau+\Delta\tau)$ by Eq. (9). Iteration would be continued on the index k until *both* the outer residual and the outer correction are small compared to ϕ_k, that is

$$\max(||\delta_k|| , ||r_{\text{outer}}(k)||) \le \epsilon_{\text{rel}}||\phi_k||+\epsilon_{\text{abs}} , \tag{12}$$

where ϵ_{rel} and ϵ_{abs} are the relative and absolute error tolerances, chosen to give some acceptable accuracy. In practice, we found that the outer correction was always small when the outer residual was and we tested Eq. (12) only for $||r_{\text{outer}}(k)||$.

When the outer convergence criterion is satisfied, $\phi(\tau+\Delta\tau)$ is set to $\phi_{k+1}(x,y)$. The accuracy of this value is then tested by an error and step-size monitor[53] which takes two successive half steps of size $\Delta\tau/2$ [starting again from $\phi_1(\tau)$] and compares the two final values for $\phi(\tau+\Delta\tau)$. If they agree to within a specified accuracy, the value is accepted, the initial value is now set to $\phi(\tau+\Delta\tau)$, and the process is repeated until a stated interval is spanned. If the two values differ too much, the integration is started again with a smaller time step (say one step of $\Delta\tau/2$ and two steps of $\Delta\tau/4$) until convergence is achieved. Although the monitor can provide effective higher-order temporal discretizations by extrapolation, we found the first-order backward Euler discretization adequate in practice. This is because only a maximum time step (independent of the solution and usually smaller than an extrapolated step) can be taken depending on the convergence properties of the inner iterative scheme used to solve Eq. (10). These convergence properties in turn depend sensitively on the particular nonlinearity and on the way the left-hand-side (lhs) operator in Eq. (10) is split to reduce the problem to the form Eq. (7). In principle, one could hope that a step-size limit could be avoided since the equation is relaxational, the evolution becomes simpler and slower over time, and ever increasing time steps should be allowed. In practice, the scheme is fast enough and the maximum allowed time step large enough for Eq. (1) to explore the interesting physics without excessive expense. An important remaining problem is to devise an implicit integration method that is fully consistent with the physical time scales of the equation.

Equation (10) is almost of the form Eq. (7) except for the nonconstant term, $-3\phi_k^2$, in the lhs operator. We can obtain the desired constant-coefficient biharmonic form if the outer correction field is the result of successive approximations of the following form:

$$\delta_k\simeq\delta_{k,m+1}=\delta_{k,m}+\eta_m , \tag{13}$$

where the inner correction field, $\eta_m(x,y)$, is assumed to be small compared to $\delta_{k,m}$ the mth approximation to δ_k. We substitute Eq. (13) into Eq. (10) and solve for η_m by splitting the operator to put the offensive term on the rhs *and* by approximating the nonconstant term acting on η_m by a constant C. We find

$$\left[L-\frac{1}{\Delta\tau}+C\right]\eta_m=r_{\text{outer}}(k)-\left[L-\frac{1}{\Delta\tau}-3\phi_k^2\right]\delta_{k,m} . \tag{14}$$

We recognize the rhs field to be the inner residual, $r_{\text{inner}}(k,m)$ of Eq. (10). This measures the extent to which Eq. (10) is satisfied after m iterations. The error in approximating $-3\phi_k^2$ by C multiplies the small quantity η_m and is dropped because this product is small compared to the other terms. Since ϕ_k is locally sinusoidal with nearly constant amplitude, a good guess for C is

$$C=-3\langle\phi_k^2\rangle\simeq-\tfrac{3}{2}||\phi_k||^2\,, \tag{15}$$

where $\langle\ \rangle$ denotes a spatial average and we have used $\langle\sin^2(x)\rangle=\frac{1}{2}$. The rate of convergence of the inner iteration scheme, Eq. (14), depends on C and is nearly optimized by the choice Eq. (15); a factor of 2 smaller or larger significantly degrades convergence.[36] Equation (14) is a constant-coefficient biharmonic problem of the form Eq. (7) (if we set $a=2$, $b=1+1/\Delta\tau-\epsilon-C$, $f_1=-r_{\text{inner}}(k,m)$, and $f_2=f_3=0$) and can be solved rapidly and accurately.[48]

How many iterations should be used to solve Eq. (14)? A natural choice is to emulate the outer convergence criterion, Eq. (12), and make the inner correction and inner residual small compared to the outer residual using similar error tolerances. A more detailed analysis[54] shows that this criterion is too stringent and wasteful since the inner equation will be solved accurately even when (for the early outer iterations) the outer equation is inaccurate. A better criterion, one that relates the inner accuracy to the current outer accuracy, is to iterate on m until the following inequality is satisfied:

$$\frac{||r_{\text{inner}}(k,m)||}{||r_{\text{outer}}(k)||}\le\alpha\left[\frac{||r_{\text{outer}}(k)||}{||r_{\text{outer}}(1)||}\right]^{\beta}, \tag{16}$$

where α and β are numbers in the interval [0,1]. Under general assumptions it can then be shown[54] that the Newton inner-outer scheme of Eqs. (8)–(16) will have $(1+\beta)$th-order convergence (so $\beta=1$ gives quadratic convergence). For moderate error tolerances of 1–10%, the rate of convergence is not sensitive to α and β; we used $\alpha=0.1$ and $\beta=0.5$ in most of our simulations.[36]

So far we have discussed only the discretization of the time derivative; any convenient method could be used to solve the resulting spatial problems. For the case of rigid boundary conditions, the residuals, corrections and the solution of the biharmonic problem,[48] Eq. (14), are all evaluated using finite differences on a discrete uniform rectangular grid of $N_x\times N_y$ points. The usual 5- and 13-point discretizations of the Laplacian and biharmonic operators are used[52] so our method is, overall, second-order accurate in the mesh spacing; doubling N_x or N_y increases the accuracy along the corresponding axis by a factor of 4. Our finite difference method does not generalize easily to circular or irregular regions because of the difficulty of interpolating the Laplacian and biharmonic operators near the boundary to second-order accuracy in the mesh size and because both operators have a singularity at the origin of a polar coordinate system. However, it is easy to generalize the scheme to allow ϵ to be both a function of space and time which would be useful for studying slow gradients[30] or periodic[55] and random modulations[56] of the Rayleigh number near onset.

Since the solution is locally sinusoidal except near boundaries and defects and no length scales significantly smaller than roll diameter (π) enter, high resolution is not needed. Numerical experiments show that 4–6 points per roll diameter (e.g., $N_x=6L_x/\pi$ and $N_y=6L_y/\pi$ where L_x and L_y are the lengths of the sides of the rectangle) provide good resolution even for defect motion. The only quantity that cannot be meaningfully calculated is the time for a stationary state to decay to another state with a lower Lyapunov value. This time is extremely sensitive to the spatial resolution, the symmetry of the state with respect to the grid points, the precision of the computer arithmetic, and the integrating accuracy.

We use three kinds of initial conditions to start the integration. The first is random initial conditions of all length scales from a mesh size up to the length of the box. Each mesh point is assigned a random value between -1 and 1 and the mesh is then smoothed to eliminate large gradients (by replacing each point by the average of itself with its four nearest neighbors and sweeping several times around the mesh). This qualitatively corresponds to uncontrolled experiments in which the Rayleigh number is *rapidly* increased from below R_c to a fixed value just above R_c. The second initial condition is a union of domains of sine functions of the same amplitude. This can generate parallel rolls of a given wave number or simple configurations of defects. Experimentally this procedure can be achieved by shining light through a mask as described by Chen and Whitehead[10] and by Pocheau and Croquette.[29] The last initial condition is to use the solution from a previous run. This corresponds to running an experiment for a while and then instantaneously jumping the Rayleigh number to a new value. Other kinds of initial conditions could have been used but were not explored, e.g., slowly increasing ϵ from below R_c to just above R_c.

The initial field, $\phi_0=\phi(x,y,\tau=0)$, was always multiplied by 10% cosine windows in the x and y directions to enforce the boundary conditions, Eq. (3a). Such a window has the form

$$w(x)=\begin{cases}1, & \alpha L\le x\le(1-\alpha)L\\ \dfrac{1}{2}\left[1-\cos\left[\dfrac{\pi}{\alpha L}x\right]\right], & \text{otherwise}\end{cases}$$

where $\alpha=0.1$ and x lies in the interval $[0,L]$. After enforcing Eq. (3a), ϕ_0 was scaled to have a mean-square value of ϵ, i.e, $\langle\phi_0^2\rangle=\epsilon$. This last condition was suggested by numerical experiments that show that the pattern evolution and the final stationary state [which is known to have an amplitude of roughly $\sqrt{\epsilon}$ by analysis of Eq. (1)] are nearly independent of the magnitude of the initial conditions. Initial conditions much smaller than $\sqrt{\epsilon}$ in magnitude evolve according to the linear equation, $\partial_\tau\phi=[\epsilon-(1+\Delta)^2]\phi$, and will grow exponentially towards $\sqrt{\epsilon}$ on a long-time scale $\epsilon^{-1}\ln(\epsilon^{1/2}/||\phi_0||)\gg1$. Similarly, for $||\phi_0||\gg\epsilon^{1/2}$, the magnitude evolves according to the equation $\partial_\tau\phi=-\phi^3$ and will decrease asymptotically as $\tau^{-1/2}$ towards $\epsilon^{1/2}$ over a time scale $(2\epsilon)^{-1}$. The expense of integrating over these long uninteresting time scales is avoided by our scaling ϕ_0 so that all three terms in Eq. (1) are balanced.

To give a feeling for the numerical complexity of the model equation, we briefly summarize the results of a typical run on a Cray-1 computer.[36] For a large aspect ratio of $\Gamma_x=30$ and $\Gamma_y=20$ (i.e., 30×20 critical roll diameters), a mesh of 193×129 points was used to give good spatial resolution, corresponding to about 6 to 7 points per

roll. (The biharmonic solver depends heavily on fast Fourier transforms[48] and N_x and N_y are chosen to be one more than a number with many prime factors.) Typical error tolerances were $\epsilon_{\rm rel}=0.10$ and $\epsilon_{\rm abs}=10^{-4}$ [see Eq. 12]. These tolerances are upper bounds in practice since our multi-iteration scheme decreases the size of the corrections and residuals so rapidly (one to two orders of magnitude per iteration) that their magnitudes are significantly smaller than the rhs of Eq. (12) when this inequality is first satisfied. A single time step by the error monitor takes typically 1 outer and 2 or 3 inner iterations provided the allowed time step never exceeds $\Delta\tau_{\rm max}\simeq 2.5$ in which case the inner iterations would fail to converge. A successful time step of 2.5 (which corresponds perhaps to 3 steps by the time-step monitor as explained above) takes 1.5 Cray-1 central-processing-unit (CPU) seconds for the given mesh. By comparison, the CPU time needed for a seven contour plot of the 193×129 mesh (see next section) takes 4—6 times as long as a single integration step. The integration would be significantly slower for a nonvector machine like a Digital Equipment Corporation VAX-11/780 minicomputer since the fast Fourier transforms and many portions of the code can be vectorized on the Cray−1.

IV. PATTERN FORMATION AND DEFECT MOTION: RIGID BOUNDARY CONDITIONS

In this section, we summarize various numerical simulations of Eqs. (1) and (3) in small- and large-aspect-ratio cells and compare the pattern evolution with experiment when possible (bearing in mind the caveats of Sec. II). For each simulation in a rectangular cell of lengths L_x and L_y, or aspect ratios $\Gamma_x=L_x/\pi$ and $\Gamma_y=L_y/\pi$, four quantities were recorded and plotted as a function of time: the Lyapunov functional, F, of Eq. (4); the maximum norm of ϕ, $||\phi(x,y,\tau)||$; the mean-square amplitude, $\langle X^2\rangle=\langle\phi^2(x,y,\tau)\rangle$; and the midpoint value, $\phi(L_x/2,L_y/2,\tau)$. The function $\langle X^2(\tau)\rangle$ is related to the Nusselt number through Eq. (6) and determines the heat flux through the cell. The midpoint value is similar to a velocity component at a particular point in the fluid that is measured experimentally by laser Doppler velocimetry.[13] Thus each simulation can relate thermal and optical measurements to the pattern evolution.[57] Every few time steps, a contour plot of the solution was calculated by linear interpolation of the field values between nearest-neighbor mesh points and contours were drawn for $0,\pm\frac{1}{2},\pm\frac{1}{4}$, and $\pm\frac{1}{8}$ the maximum norm of the field. The simulation was continued until $|(1/F)(dF/d\tau)|\lesssim 10^{-8}$ at which point we assumed the solution was stationary to good accuracy.

Before discussing our results, we define a little more precisely what is meant by "close to onset" to remove any ambiguity between our numerical runs and experiment. For finite cells, the critical reduced Rayleigh number, ϵ_c (above which the zero solution representing conduction becomes unstable to nonzero convection solutions), is finite instead of zero because of the damping influence of the lateral walls. ϵ_c can be obtained by solving the linear eigenvalue problem[25]

$$(\Delta+1)^2\phi=\epsilon\phi\ ;\quad \phi=\partial_n\phi=0,\ \text{on boundaries} \tag{17}$$

for the smallest positive eigenvalue (corresponding to a symmetric eigenfunction). An approximation to ϵ_c can be found[58] by assuming an aspect ratio is small (say Γ_x) and solving a one-dimensional problem on the interval $[-L_y/2,L_y/2]$. This should be valid for $\Gamma_y\gg\Gamma_x$ or for $\min(\Gamma_x,\Gamma_y)\gg 1$. It is easily seen that the lowest eigenvalue is then the smallest positive root of the transcendental equation

$$(1+\sqrt{\epsilon})^{1/2}\tan\left[\frac{L_y}{2}(1+\sqrt{\epsilon})^{1/2}\right] =(1-\sqrt{\epsilon})^{1/2}\tan\left[\frac{L_y}{2}(1-\sqrt{\epsilon})^{1/2}\right], \tag{18}$$

with eigenfunction

$$\phi_c(x,y)=A_+\cos[(1+\sqrt{\epsilon})^{1/2}x]+A_-\cos[(1-\sqrt{\epsilon})^{1/2}x]\ .$$

The solution of Eq. (18) is presented numerically in Fig. 3 where ϵ_c is plotted versus $\Gamma=\Gamma_y$. For $\Gamma\gtrsim 5$, ϵ_c is approximated accurately by the asymptotic formula[59]

$$\epsilon_c\simeq\left[\frac{2}{\Gamma}\right]^2,\quad \Gamma\gg 1\ . \tag{19}$$

[This simple inverse quadratic dependence on Γ, Eq. (19), does not seem to have been recognized in an earlier more sophisticated study of Eq. (17) by Davis[60] or by Stork and Müller[9] who find a similar result.] For smaller Γ, ϵ_c in Fig. 3 is a lower bound to the correct value since the finite size of the perpendicular direction will increase ϵ_c. Rough estimates for small cells can be obtained independently by solving Eqs. (1) and (3a) with random initial conditions for different values of ϵ. In this way, it was found that Fig. 3 is accurate even for square cells of aspect ratio $\Gamma\gtrsim 4$ and seriously underestimates ϵ_c for $\Gamma_y\lesssim 2$ independently of how large Γ_x is.

For our purposes, close to onset will mean

$$\epsilon_c<\epsilon<1.2\epsilon_c\ ,$$

where ϵ_c can be found from Fig. 3 or Eq. (19). From the discussion in Sec. II, this is the range (for large cells) in which two length scales enter Eq. (1), $2\pi/k_c=2\pi$ and the

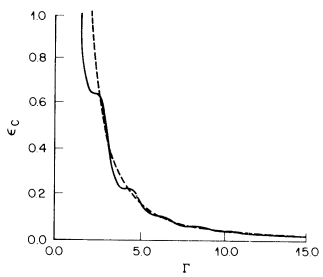

FIG. 3. Critical reduced Rayleigh number for a finite channel ϵ_c vs the aspect ratio Γ. The dashed curve is the asymptotic large-Γ formula for ϵ_c, $(2/\Gamma)^2$, Eq. (19). ϵ_c gives a good approximation to the true ϵ_c for a rectangular cell of aspect ratio Γ_x and Γ_y when $\min(\Gamma_x,\Gamma_y)\gtrsim 4$.

healing length of order $(\epsilon-\epsilon_c)^{-1/2}$. Close to onset, when $(\epsilon-\epsilon_c)^{-1/2}\simeq\min(\Gamma_x,\Gamma_y)\gg 1$, pattern formation consists of parallel rolls without defects and is not interesting. Far from onset, when $(\epsilon-\epsilon_c)^{-1/2}\simeq 1$ and only one length scale enters, our model equation is no longer obviously related to the Boussinesq equations. Most experiments to date have not been close to onset because of the inconvenient critically-slowed-down time scale.

A. Small- and medium-size cells

Using this criterion, we first made several runs close to onset in small- and medium-aspect-ratio cells with cell dimensions identical to those used by Stork and Müller in their optical variable-aspect-ratio experiments.[9] These authors slowly increased R from below to just above R_c and photographed the resulting stationary states; they unfortunately did not report the heat flux or final Rayleigh number which makes comparison with our calculations (Figs. 4—8) difficult. For cells with a side less than a roll diameter, Fig. 4, we find two kinds of stationary states depending on the initial conditions. Parallel rolls of the critical wavelength lead to Fig. 4(a) which agrees with Fig. 6(a) of Stork and Müller. However, random initial conditions lead to a lower solution [F, from Eq. (4), is lower in Fig. 4(b)] which seems unphysical because of the broken symmetry with more positive than negative field. For even smaller sides (not shown), the lowest Lyapunov state near onset is positive everywhere (although oscillating solutions occur at higher ϵ). These solutions occur only

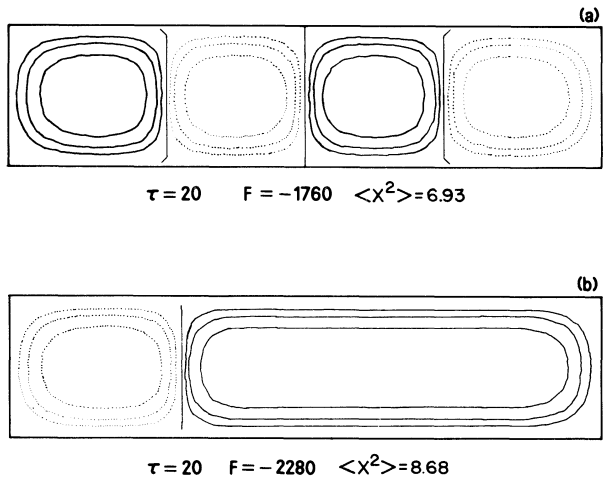

FIG. 4. Contour plots of the stationary solutions of Eqs. (1) and (3) for an extremely small cell of aspect ratio $\Gamma_x=4$, $\Gamma_y=1$. The contours are plotted for 0, $\pm\frac{1}{2}$, $\pm\frac{1}{4}$, and $\pm\frac{1}{8}$, times the maximum absolute value of $\phi(x,y,\tau)$. This quantity differs from cell to cell, and contours in (a) do *not* correspond exactly to the values of contours in (b). Value of ϵ was 25 for both cases and a uniform rectangular mesh of 33×17 points was used. The quantities τ, F, and $\langle X^2\rangle$ are, respectively, the final integration time [in the time units of Eq. (1)]; the value of the Lyapunov functional, Eq. (4); and the mean-square field $\langle\phi^2(x,y,\tau)\rangle$. (b) has the lower value of F.

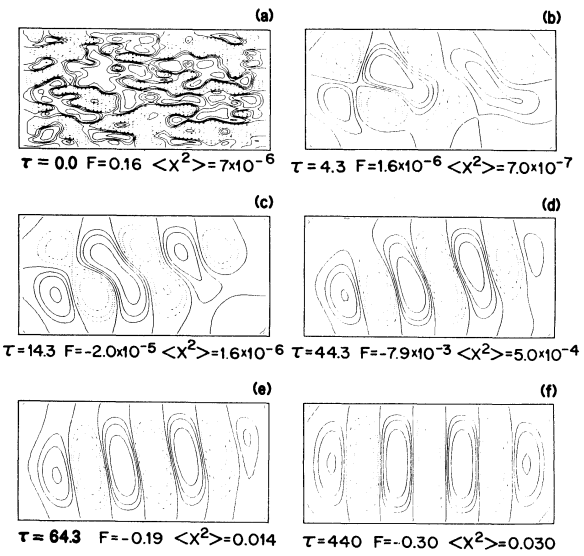

FIG. 5. Example of pattern formation starting from random initial conditions in a small rectangular cell of aspect ratio $\Gamma_x=8$ and $\Gamma_y=4$; a 65×65 mesh was used and $\epsilon=0.18$. The Lyapunov functional F steadily decreases while the mean-square amplitude $\langle X^2\rangle$ steadily increases throughout the integration. The final stationary state (f) has 7 rolls and is metastable. It can decay in the presence of large fluctuations to an 8-roll state of lower F value.

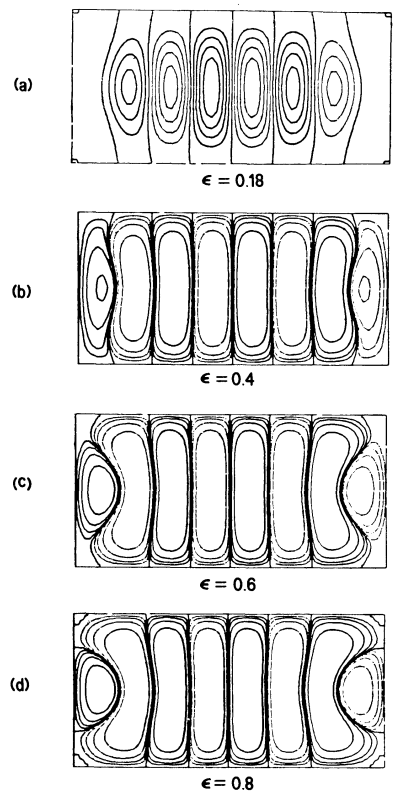

FIG. 6. Dependence of roll boundaries of stationary states on the reduced Rayleigh number for the cell of Fig. 5. As ϵ is increased, the rolls nearest the side walls become increasingly distorted. The initial condition was $\sqrt{\epsilon}\sin(x)$ for all four cases (i.e., parallel rolls of the critical wavelength, $k_c=1$).

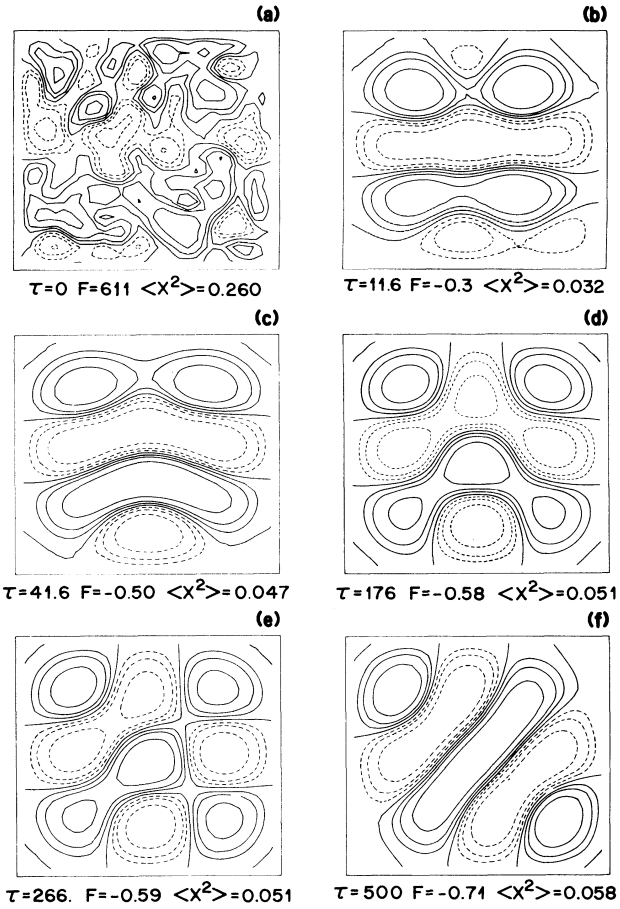

FIG. 7. Example of pattern formation starting from random initial conditions in a small nearly square cell of aspect ratio $\Gamma_x=5.0$ and $\Gamma_y=4.7$, to compare with the experimental cell of Stork and Muller (Ref. 9; their Fig. 7F). Mesh size is 33×33 and $\epsilon=0.30$. The random initial values evolve to a metastable stationary state (d), which is a superposition of crossed rolls. Numerical noise breaks the symmetry (e) and leads to the stationary state (f). The time for (d) to evolve to (e) depends sensitively on numerical details of accuracy and mesh size and is not physically significant.

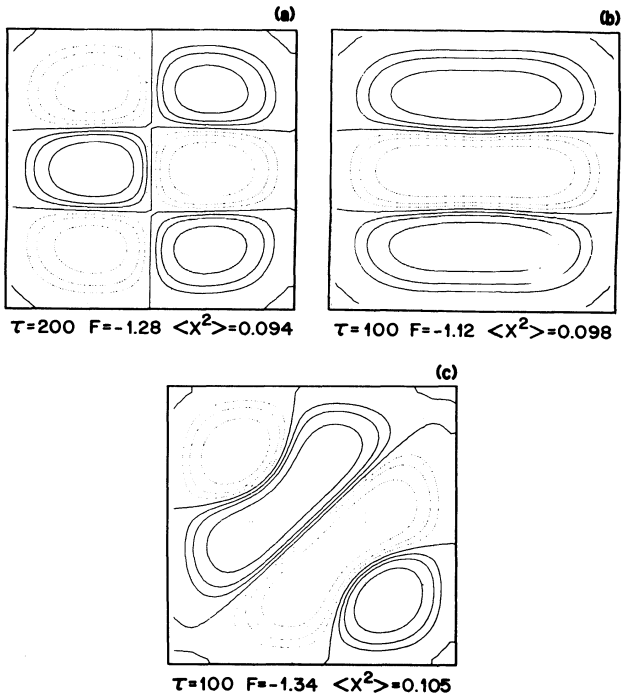

FIG. 8. Final stationary states in a small square cell of aspect ratio $\Gamma_x=\Gamma_y=4$. A mesh size of 25×25 was used and $\epsilon=0.50$. State (a) started from parallel rolls of the critical wavelength while states (b) and (c) started from random initial conditions. Repeated runs with different initial conditions always lead to one of these three states; the degeneracy of solutions near onset is small. State (c) is the most stable state while states (a) and (b) are metastable. The maximum heat transport occurs for the most stable state, (c).

for small cells [$\min(\Gamma_x,\Gamma_y)\lesssim 2$]. They reflect the lack of any conservation law forcing the field ϕ to have a mean value of zero in our model; the incompressibility of the fluid does not enter at this level of the amplitude equation. For larger cells, the field always seems to evolve to a state of mean zero even if the initial conditions do not have this property. We note that the lower solution, Fig. 4(b), also has the larger heat flux or mean-square amplitude, $\langle X^2\rangle$. This is a general feature of Eq. (1) which we discuss further below.

Representative evolutions in small cells starting from random initial conditions are given in Figs. 5, 6, 7, and 8. In Fig. 5(a), we see that the short- and long-length scales anneal out rapidly on a time of order 1, leaving positive and negative domains of size $2\pi/k_c$ [Fig. 5(b)]. This is a result of the strong filtering effect of the linear operator $\epsilon-(1+\Delta)^2$ which forces all wave numbers to lie in the neutral stability region $\epsilon-(1-k^2)^2\geq 0$. These domains evolve under the influence of the lateral walls, elongating, merging, and orienting to become parallel to the shorter side and perpendicular to the long side. The rolls are not perpendicular to the nearest sides during the evolution, at least on a length scale[61] of order $2\pi/k_c$. This feature of the rolls evolving to become parallel to the shorter side was predicted long ago from a linear stability analysis[60] but is understood simply in the nonlinear regime by the arguments of Cross.[8] The final state has seven rolls and has a higher-Lyapunov value compared to the eight-roll state [shown in Fig. 6(a)] obtained by starting from parallel rolls of $k=k_c$ (F is then -0.38).

Repeated runs with different random initial conditions always lead to a seven-or eight-roll state as in Figs. 5(f) and 6(a). While a uniform seven-roll state is consistent with the wave-number selection predicted by the linear stability analysis of Sec. VI, a wave number of $\frac{7}{8}$ lies outside the much smaller stable region predicted for one-dimensional geometries by the deeper analysis of Refs. 33 and 34; for Eq. (1) in one dimension, only wave numbers lying within the band $|k-1|\leq\epsilon/16$ are stable. A careful examination of Fig. 5(f) shows that this criterion is not violated *because the local wave number is not uniform.* It varies from less than $\frac{7}{8}$ near the sidewalls to 1 (within numerical accuracy) at the center of the cell.[62] This supports the analysis of Refs. 33 and 34 and suggests that the

presence of corners does not affect their one-dimensional results. Further experimental and numerical work would be useful to investigate this more thoroughly.

The mild curvature of the rolls closest to the smaller sides in Fig. 5(f) agrees with experiment [see Fig. 6(d) of Ref. 9] and shows that the experimental curvature is not an artifact arising from engineering imperfections (such as a small horizontal temperature gradient). Instead it arises from the presence of corners. Other experimental patterns of Stork and Müller[9] [see their Figs. 5(c),6(g),7(f)], especially in small square cells, are not found among the solutions of Eqs. (1) and (3). These may well be due to small horizontal temperature gradients. A ϵ is increased from ϵ_c, the bending of the rolls nearest the side walls increases, from straight rolls to rolls bending nearly 90° (see Fig. 6). The roll pattern of Fig. 6(d) has not been observed experimentally. It is the first of several clues that Eq. (1) becomes a poor approximation to the Boussinesq equations for $\epsilon \gtrsim 1$.

In a square or nearly square cell, the degeneracy and symmetry are higher and the evolution is more complicated (Figs. 7 and 8). Some random initial conditions [Fig. 7(a)] evolve to a state [Fig. 7(d)] which is quiescent for 90 time units after which integration errors break the symmetry and a lower stationary state appears with rolls oriented along the diagonal [Fig. 7(f)]. The complex pattern, Fig. 7(d), is similar to several patterns observed by Stork and Müller [see their Figs. 7(g) and (9)] although it is not clear from experiment whether their rosette shapes are unstable to rolls oriented along the diagonal as in our Fig. 7(f). The arguments of Schlüter, Lortz, and Busse[63] suggest that, for large cells and near onset, superpositions of rolls of the kind giving Fig. 7(d) are unstable to locally single rolls. However superpositions may be stabilized by close lateral walls. The possible degeneracy of these square cells can be explored by repeated integrations starting from different random initial conditions or parallel rolls and is shown in Fig. 8. Figure 8(a) is a state arising from parallel x rolls while Figs. 8(b) and 8(c) arise from random initial conditions. Different runs on this cell always lead to one of these three states so the degeneracy is small; none of the stationary states are simply related to the linear eigenfunctions[25] of Eq. (17). The globally stable state is a single set of rolls oriented along the diagonal which also maximizes the heat transport.

The results of Figs. 4—8 and other integrations not shown reproduce nearly all the experimental observations of Stork and Müller.[9] The exceptions are cells with a side smaller than $2\pi/k_c$ and small square cells for which small horizontal temperature gradients may stabilize the experimentally observed pattern. Stork and Müller found a tendency for rectangular cells to prefer an even number of rolls. This tendency does not appear in the Lyapunov functional, Eq. (4). Instead, small horizontal temperature gradients could be the source of this bias. It would be interesting to repeat some of these experiments more carefully to test the ordering by the Lyapunov functional of the various patterns (perhaps by shining a focused beam of light to break some symmetry) and to check if the most stable pattern always has the largest heat flux, if the most stable pattern is not a superposition of rolls, and how far above ϵ_c these observations remain true. Other experiments in small cells by Gollub, Benson, and Steinman[64] show asymmetric patterns involving a small roll near a corner. This may be because of experimental imperfections or because more complicated states are stable away from onset in the real system. The issue is important since further bifurcations leading to turbulence depend sensitively on the initial spatial state near onset.[13] Equations (1) and (3) could provide a way of classifying these states for moderate sized cells, at least near onset.

B. Large rectangular and square cells

The evolution in large-aspect-ratio cells involves the presence and interaction of roll imperfections and is generally more complicated (Figs. 9—24). The simplest case is the evolution of parallel rolls of the critical wavelength in large rectangular and square cells (Fig. 9). We see that the rolls parallel to the side wall are unstable to cross rolls (also of the critical wavelength) which grow only a finite distance in from the boundaries. This is so even though the resulting stationary state often has a higher-Lyapunov value than a state of more complicated symmetry.[26] This

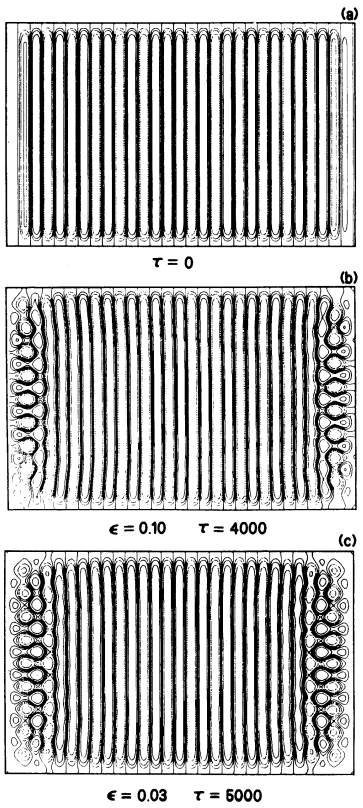

FIG. 9. Pattern formation in a large rectangular cell of aspect ratio $\Gamma_x = 29.2$ and $\Gamma_y = 19.5$ to match the experimental cell of Ref. 19. The initial conditions are parallel rolls of $k = k_c = 1$ and a 193×129 mesh was used. For small ϵ, the rolls parallel to the shorter side are unstable to cross rolls of the critical wavelength, (b). The cross rolls only grow in a finite extent over a healing length of magnitude $(\epsilon - \epsilon_c)^{-1/2}$. Decreasing ϵ, state (c), increases reversibly the length of the cross rolls. States (b) and (c) are stationary for $\tau \gtrsim 500$.

linear instability to cross rolls was first predicted by Pomeau and Zaleski[35] and has been observed in several experiments.[10] Pocheau and Croquette have also induced cross rolls that extend beyond the boundary layer by a shadow-graph technique.[29] They find that such cross rolls provide an efficient mechanism for wave-number selection in the interior of the cell. Since $k_c = 1$ is the preferred wave number in our model (see Sec. VI) and the simulations in Fig. 9 start with this wave number, no selection occurs. The instability affects only the rolls within a boundary layer of size $(\epsilon - \epsilon_c)^{-1/2}$ from the side walls, on a time scale $\tau \lesssim 500$. It is not known if cross rolls spontaneously induced by the presence of corners, as in Fig. 9, can also provide a selection mechanism.

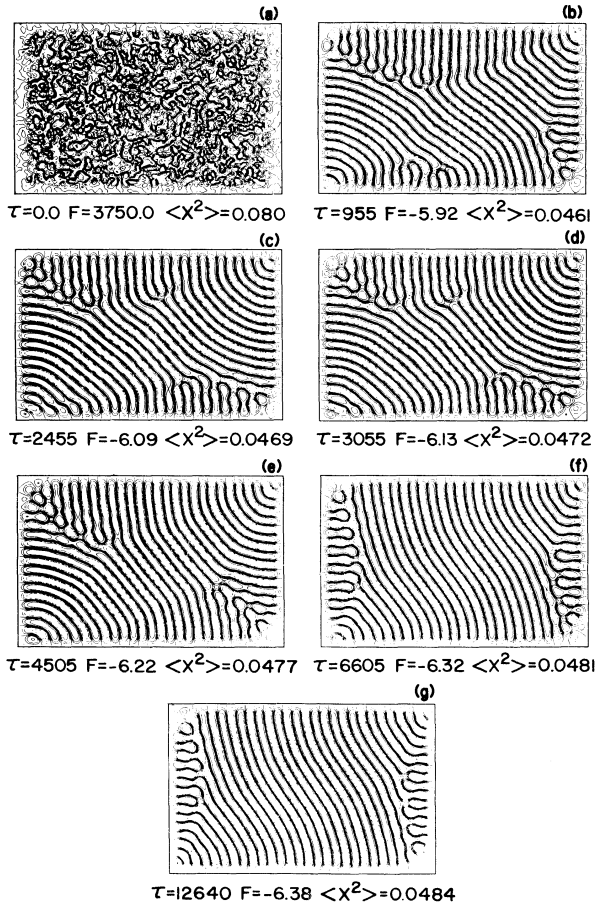

FIG. 10. Pattern formation starting from random initial conditions (a) for the same cell size as Fig. 9. The same 193×129 mesh was used and $\epsilon = 0.10$. The random initial conditions anneal out to give domains of rolls close to the critical wavelength that are linked by various kinds of defects such as grain boundaries, dislocations, and disclinations, (b). The rolls are already perpendicular to all boundaries except near corners, and defects have migrated away from or annihilated in the center of the cell, leaving a locally uniform patch. Successive evolution involves dislocation gliding, clear examples of which are seen along the bottom wall of (b), (c), and (d) (towards the right corner) and vertically upwards on the right wall, (e) (f), and (g). Concentric rolls around a corner form early in the evolution but eventually disappear. The evolution becomes stationary after $\tau \cong 12\,000 \simeq 30$ horizontal-diffusion times, τ_h. The final state is remarkably similar to Fig. 9(b). The numerical evaluation of F for the given mesh is not accurate enough to state definitively whether (g) is lower than Fig. 9(b) (for which $F = -6.33$). State (g) has not been seen experimentally.

Figures 10—14 show the spatial and temporal evolution from random initial conditions in large rectangular cells near onset. These differ considerably from the evolution already described in Fig. 5. In Fig. 10, we see that the small- and large-length scales anneal out rapidly leaving a high density of defects [Figs. 10(b) and 11(a)]. The rolls are perpendicular to all boundaries but only on a length scale of a roll diameter, beyond which they bend or curve rapidly, leading to a disordered texture in the center of the cell. Figure 10(b) has roughly concentric rolls at the lower left and upper right corners with the corners as focus. Domains of one orientation [e.g., the vertically oriented rolls emerging from the top of the cell in Fig. 10(b)] meet domains of another orientation at an abrupt angle, creating a grain boundary. Further evolution consists *primarily* of defects and dislocations gliding perpendicular to the local roll axis towards corners or towards the shorter side. This is seen clearly in the bottom of Figs. 10(b), 10(c), and 10(d) in which dislocations glide towards the right lower corner, merging or annihilating to give Fig. 10(e). Although Fig. 10(e) has a pleasing symmetry, it is still evolving to Figs. 10(f) and 10(g), a stationary state in which all defects have been eliminated from the center of the cell.

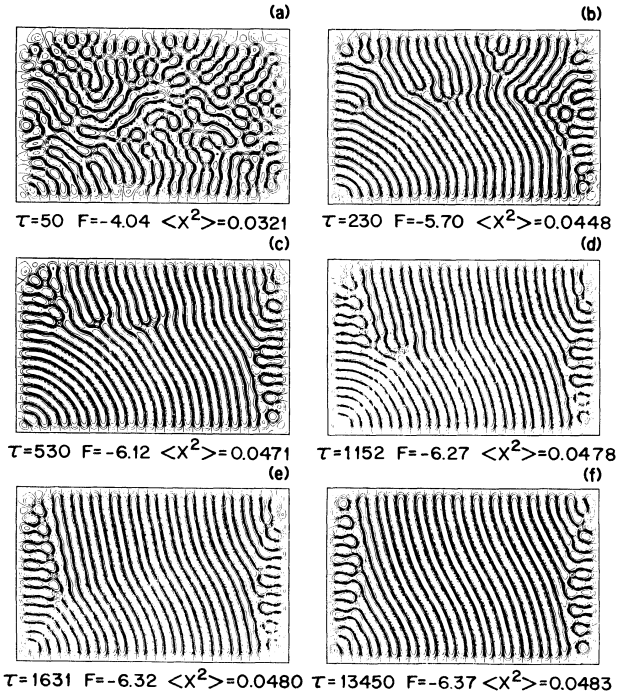

FIG. 11. An evolution identical to Fig. 10 except a different random seed was used to create the random initial conditions. (a) shows the greatly disordered pattern shortly after the annealing of short- and long-length scales. Although the succeeding evolution differs in details from Fig. 10, the final stationary state is almost identical, suggesting that there is a unique state accessible by random initial conditions close to onset in large cells.

This final state is similar to Fig. 9(b). Indeed, the Lyapunov functional value for Fig. 10(g), $F=-6.38$, is not significantly lower numerically than that of Fig. 9(b), $F=-6.33$. Recent arguments by Zaleski *et al.*[65] suggest that the curved rolls of Fig. 10(g) give a lower Lyapunov value per unit length than straight rolls in the limit of infinitely long cells, i.e., a channel, and possibly explain our numerical results. A similar run with different random initial conditions is given in Fig. 11; the first panel shows the highly disordered field shortly after the annealing of the random initial conditions. The evolution differs in many details from Fig. 10, e.g., a concentric set of rolls never appears on the upper right corner, no defects glide on the lower horizontal boundary and the time scale to become stationary is much smaller. However, the final state is almost identical to Figs. 10(g) and 9(b), suggesting that arbitrarily complicated configurations of defects [Fig. 11(a)] can simplify and evolve to a unique most-stable state. This is true only close enough to onset and for large enough cells. Experiments[19,29] and simulations for larger ϵ show that the evolution is more constricted further away from onset, as we discuss later.

The time dependence of several experimentally related quantities is given in Fig. 12, corresponding to the first 3000 time units of Fig. 10. All four curves show a sharp change over the first 50 time units as the large gradients of the random initial conditions anneal out. The Lyapunov functional, Fig. 12(a), decreases exponentially over the first 500 time units and then decreases roughly linearly until the pattern becomes stationary ($\tau\simeq 12\,000$ in Fig. 10). The steady monotonic decrease of F is a measure of the validity of the numerical integrating scheme since F must mathematically decrease and become stationary for all initial conditions.[8] (In runs in which the mesh gave poor resolution, the Lyapunov functional was found often to decrease and then slowly increase.) A careful examination of the data in Fig. 12(a) and its extension to later times shows that F *steadily* decreases (the slope is nowhere zero). The long-time scale found in Figs. 10 and 11 (and later figures) does not arise from noise-induced transitions over a barrier to a lower state provided the cell is large enough (see e.g., Fig. 7, a small cell that *does* involve a noise-induced transition). More precisely, Fig. 12(a) shows that there are no barriers comparable with the integrating accuracy; we cannot completely rule out that states such as Fig. 10(e) might be metastable in the limit of a fine mesh. This is unlikely since the pattern has no particular symmetry with respect to the underlying mesh.

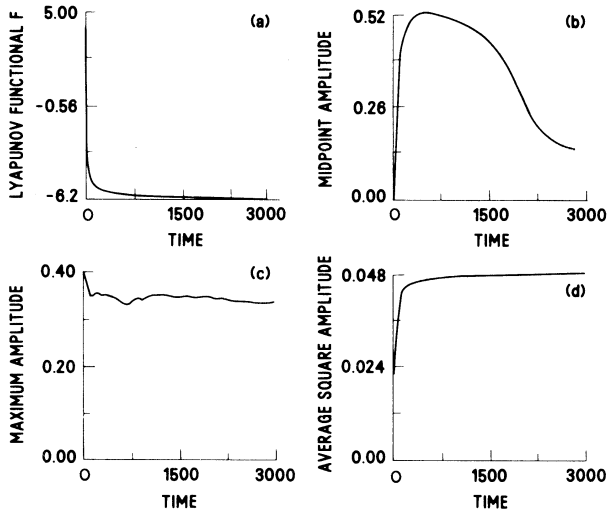

FIG. 12. Time dependence of the Lyapunov functional, maximum, midpoint, and average-square field for the first 3000 time units of Fig. 10. The smooth dependence in (b) reflects the absence of defects in and near the center of the cell.

Figure 12(b), the midpoint field, corresponds to the measurement of a velocity component on some plane in the middle of the cell. The slow featureless time dependence (compare Fig. 3 of Ref. 19) is common for large cell simulations near onset. It corresponds to defects rapidly moving away or annihilating from the center of the cell, leaving a locally uniform patch of rolls which rotates slowly back and forth around some point near the center as the pattern continues to evolve. A point closer to the boundary or near a corner would give a more complicated time dependence on a more rapid time scale. An example of this is given in Fig. 10(c) which shows how the maximum norm, $||\phi(x,y,\tau)||$, evolves in time. Because of the way the initial conditions were scaled (see discussion in Sec. III) the maximum absolute value changes little from the expected value of $\epsilon^{1/2}=(0.1)^{1/2}\simeq 0.32$. The small fluctuations, on a time scale fast compared to Fig. 12(b), correspond to the motion or annihilation of defects near the point where the current maximum occurs.

Figure 12(d), the average-square amplitude, $\langle\phi^2(x,y,\tau)\rangle=\langle X^2\rangle$ is the vertical heat transport as a function of time [see Eq. (6)]. This quantity steadily and monotonically increases with no obvious fluctuations arising from defect motion or annihilation. This contrasts strongly with the time evolution seen near onset in large cylindrical cells that shows 1—3% fluctuations in the Nusselt number as a function of time.[16,17] Unlike the Lyapunov functional, there is no particular mathematical reason for $\langle X^2\rangle$ to increase monotonically from the initial conditions or to be a maximum for the most stable state as we have consistently observed in large cells. Indeed, when $\langle X^2\rangle$ is calculated for the evolution of a small cell [$\min(\Gamma_x,\Gamma_y)\lesssim 2$], it is often found to decrease, ruling out the possibility that this *is* a general feature. There is an extremum principle of Busse[66] which applies to Eqs. (1) and (3) for small ϵ and could explain the monotonic increase close to onset. However, behavior similar to Fig. 12(d) is found for both small and large ($\epsilon\gtrsim 1$) values of ϵ for large cells at least asymptotically for large time. Figure 12(d) suggests a simple way to determine when Eqs. (1) and (3) can be related to experiment. Such an experiment in a medium-aspect-ratio cylindrical cell was recently tried by Walden who found the results of Fig. 13 close to onset. The Nusselt number undulates in a complicated way before settling down to a stationary state. The behavior does become simpler closer to onset ($\epsilon\lesssim 0.3$) and reasonable agreement with Fig. 12(d) is obtained after the decay of the transient arising from the rapid change in ϵ. Better agreement might be found for larger rectangular cells and closer to onset; this should be studied further.

How much does the evolution and time dependence

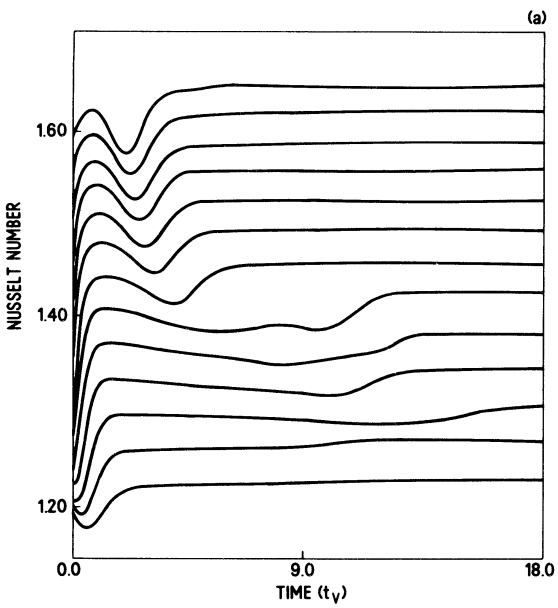

FIG. 13. Experimental time dependence of the Nusselt number for different fixed heat currents in a small cryogenic cylindrical cell of aspect ratio $\Gamma=D/2d=2.93$, where D is the diameter and d is the fluid depth of the cell. The Rayleigh number was measured and converted into the Nusselt number (Ref. 18). The cell was repeatedly held at subcritical heat currents (roughly $0.9R_c$) for about 10 vertical diffusion times and then, at $t=0$, the heat current was instantly increased to supercritical values ranging from $1.1R_c$ to $1.7R_c$ in 5% increments. Although the heat transport always became stationary, it did not relax monotonically to the stationary value except very close to onset (near 1.20 on the vertical axis). The transient is more complicated than that found in simulations of Eqs. (1) and (3) for square cells of comparable size ($\Gamma\simeq 5$). The corresponding experimental flow visualization is not known. We are indebted to R. Walden for this data.

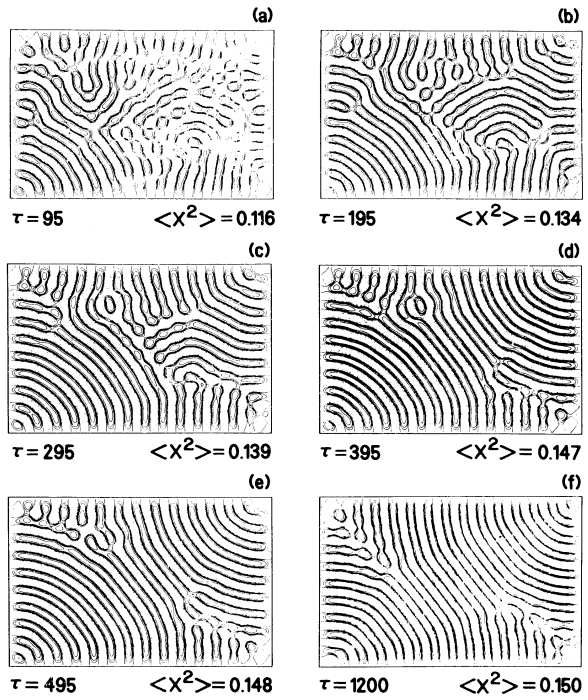

FIG. 14. Pattern formation starting from random initial conditions for Eq. (20), a nonrelaxational form of Eq. (1). The same cell, mesh size, and ϵ values as Figs. 10 and 11 were used. The evolution for $\tau\gtrsim 400$ is remarkably similar to Fig. 10, suggesting that for $\epsilon=0.10$ the equation is close enough to onset that the dynamics follow the same (variational) amplitude equation to which it reduces in perturbation theory. An interesting detail is the spontaneous creation of an isolated defect in (b)–(d). This is probably not unique to Eq. (20). (f) is *not* stationary and evolves to a state identical to Fig. 9(f). The mean-square amplitude increases monotonically throughout the integration.

[particularly Fig. 12(d)] depend on the variational form of Eqs. (1) and (3)? The answer is not much. Figure 14 shows an evolution similar to Fig. 10 for the equation

$$\partial_\tau\phi=[\epsilon-(\Delta+1)^2]\phi-\phi(\vec{\nabla}\phi)^2\ , \tag{20}$$

which is *not* rigorously relaxational. The evolution differs only in minor details from Fig. 10. The flow becomes stationary, the heat transport increases monotonically and becomes steady just as in Fig. 12(d), and the kinds of patterns are similar [compare Fig. 14(f) with 10(e)]. The boundaries clearly dominate the pattern formation, forcing the rolls to be perpendicular to the walls and forming concentric rolls around corners. Further integrations of Eq. (20) in much larger cells ($\Gamma\gtrsim 60$) would be useful to prove conclusively that a nonperiodic time dependence does not occur simply because Eq. (20) is not relaxational. It should be kept in mind, however, that the clear time dependence in some experiments[19] seems to be related to the skewed-varicose instability which does not occur in Eq. (1) or its nonrelaxational forms, Eqs. (20).[67]

The discussion so far has concentrated on large rectangular cells in which the roll orientation eventually becomes parallel to the shorter side [compare Figs. 5(f) and 10(g)]. We have made similar calculations in large square cells to study the effect of a greater spatial degeneracy and to extend the results of the smaller cells of Figs. 7 and 8. Figure 15 shows the evolution from random initial conditions [15(a)] to the final stationary state [15(f)]. The first surprising result is that the time scale for the pattern to become stationary is much longer than that of the rectangular cells of Figs. 10, 11, and 12 although the latter are much larger; the higher symmetry of the square box leads to more complicated longer-time-scale flows. This suggests that the evolution of Eq. (1) in a cylindrical cell of comparable size should take even longer. We see that the rolls again evolve at an early stage [Fig. 15(b)] to be perpendicular to all boundaries leading to defects and grain boundaries. Defects rapidly move or disappear from the center of the cell leaving a patch of regular rolls that rotate back and forth as the evolution continues. The evolution is similar to Fig. 10 in that concentric rolls form around diagonally opposite corners, defects (mainly dislocations) glide to nearby corners and merge with other defects, and disclinations tend to form at these corners [compare Fig. 10(e) with 15(e)]. The final state has rolls oriented predominantly along the diagonal [and in this

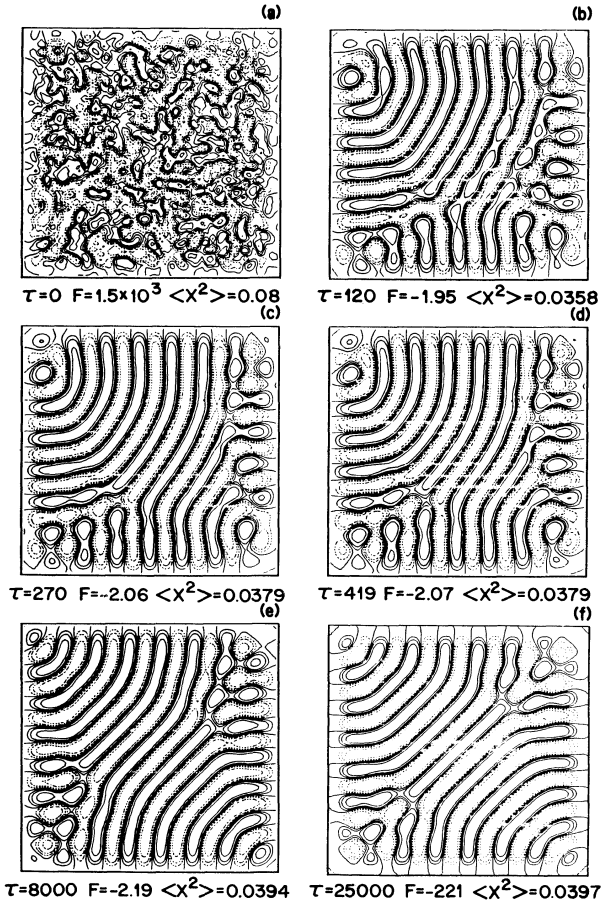

FIG. 15. Pattern formation starting from random initial conditions (a) for large square cells (here $\Gamma_x=\Gamma_y=16$, $\epsilon=0.10$, and a 97×97 mesh was used). The evolution is similar to that in rectangular cells (Figs. 10, 11, and 14) except that the time scale to become stationary is substantially longer ($\simeq100\tau_h$), even though the lateral dimension is smaller. (e), similar to Fig. 10(g), evolves to the highly symmetric stationary state (f). The sharp bending of the rolls away from the boundaries is an unexpected feature. (f) has a lower Lyapunov value than the state obtained from parallel rolls as initial conditions (Ref. 26).

sense is similar to Figs. 7(f) and 8(c) for smaller aspect ratios] with concentric rolls along opposite corners and two dislocations aligned along a diagonal. This state has a lower Lyapunov value than the state obtained by starting from parallel rolls[26] as in Fig. 9. Indeed, another run starting from different random initial conditions also leads to Fig. 15(f), suggesting that this may be the unique globally stable state for this value of ϵ. A curious feature of Fig. 15, already mentioned in Ref. 26, is that away from the boundaries, the rolls bend abruptly, yielding a domain of straight rolls in the center of the cell. This feature is not restricted to the onset region and remains true even for larger ϵ. It is not clear whether such behavior is seen experimentally or whether a smoother bending is prevalent.

Starting with exactly the same initial conditions as in Fig. 15(a) but with a value of ϵ not close to onset, qualitatively different pattern formation is observed (Fig. 16). The rolls do not immediately evolve to be normal to the boundaries, defects do not migrate away from the central region, rolls curve over much larger angles, the defect density remains much higher throughout the evolution, and the pattern becomes stationary on a more rapid time scale ($\simeq25\tau_h$). Figure 16 suggests that away from onset, barriers to defect motion appear or become larger and dislocation gliding no longer takes place. The pattern is disordered and rigid, and probably is one of many local minima possible for the Lyapunov functional, Eq. (4). The global minimum is likely to be the symmetric state of parallel rolls.[26] The large angles over which some of the

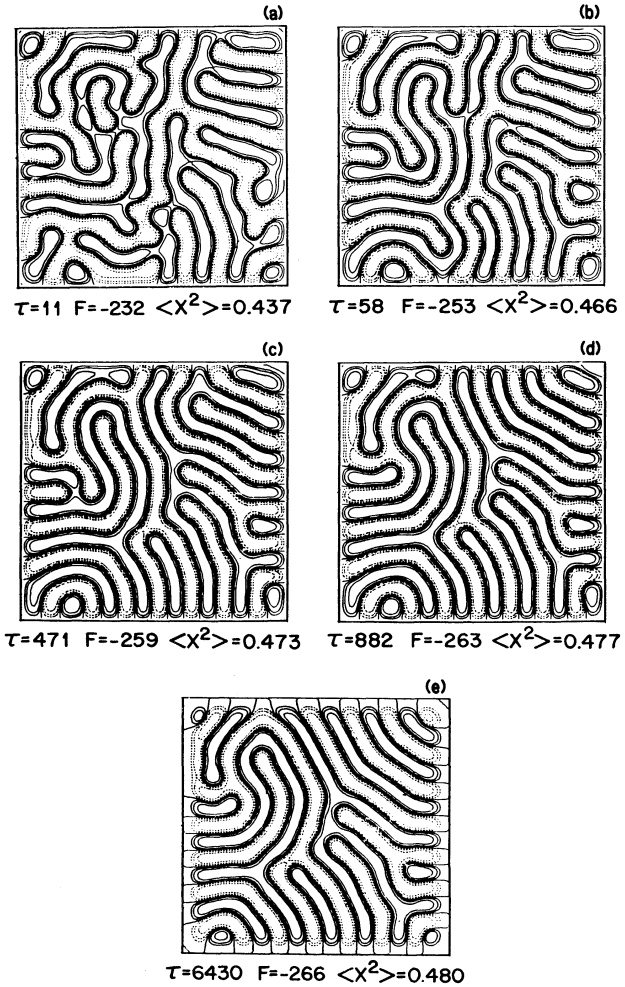

FIG. 16. Pattern formation, *not* close to onset, starting from random initial conditions. Same initial conditions and parameters as Fig. 15 were used except ϵ was set to 0.90. Evolution is rigid, with many defects that move only short distances by the time the pattern becomes stationary in (e). Rolls do not come in perpendicular to all walls and they bend over large angles; defects do not migrate or disappear near the center of the cell. Time scale to become stationary ($25\tau_h$) is substantially smaller than Fig. 15. Mean-square amplitude still monotonically increases.

rolls bend [e.g., the loop near the upper left corner of Figs. 16(b)–16(c) can be explained by the larger band of stable wave numbers out of which the pattern can be constructed (see Sec. VI]. This rigid disordered pattern can be understood in more detail by a few simple experiments (Fig. 17). If Fig. 16(e) is used as the initial conditions for a run with $\epsilon=0.10$, the pattern changes significantly [Fig. 17(c) to 17(d)] and eventually evolves to a state identical to Fig. 15(f) for $\tau \gtrsim 10000$, not shown. This is because, for smaller ϵ, the amplitude must go to zero in regions where the rolls bend sharply (involving wave numbers outside the stability band for $\epsilon=0.10$). Also inside the now larger core region of size $(\epsilon-\epsilon_c)^{-1/2}$, the rolls can rearrange in a more favorable manner. The reverse experiment consists of using the stationary state, Fig. 17(a), as the initial conditions for a run with $\epsilon=0.90$. Here the evolution is trivial and the same pattern is obtained [Fig. 17(b)]. The rolls still bend abruptly away from the boundary verifying that this bending is not related to the presence of boundary layers (which are now smaller than a roll diameter). The state, Fig. 17(b), has a higher Lyapunov value than that obtained by starting from parallel rolls.[26] Far from onset, the most symmetrical state seems always to have the lowest value, but is not easily attained from random initial conditions.

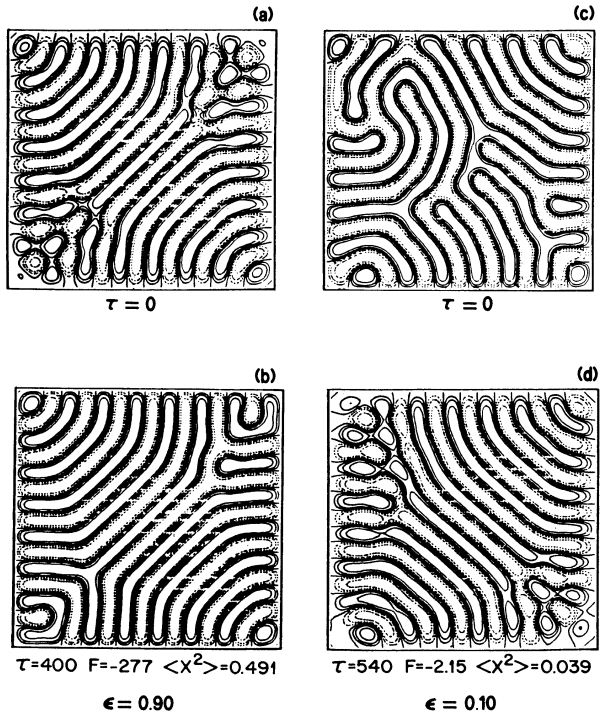

FIG. 17. Numerical experiments to test pattern stability. If the stationary state of Fig. 15(f), shown in (a), is used to start a run at $\epsilon=0.90$, the state immediately becomes stationary as in (b); this state in turn has a higher F value than the one obtained starting from parallel rolls (Ref. 26). This demonstrates that symmetric patterns like the latter are likely to be globally stable for $\epsilon=0.90$. If the stationary state of Fig. 16(e), shown in (c), is used to start a run with $\epsilon=0.10$, the pattern rapidly "melts" and evolves towards (a), as in (d). Defect motion is impeded for larger values of ϵ.

An extreme example of the constrained evolution for larger ϵ is given in Fig. 18, starting from the same initial conditons as Fig. 10(a), but with $\epsilon=2.0$. There is no longer any tendency for rolls to evolve perpendicular to the boundaries, the density of defects is high and constant, and the stationary state, Fig. 18(e), is attained rapidly compared to Figs. 10, 11, and 14. The final pattern bears no resemblance to any known Rayleigh-Bénard experiment and suggests that the model equation is not applicable for $\epsilon \gtrsim 1$. Figure 18 does resemble patterns in other systems such as magnetic bubbles[68] or ferrofluids.[69] Equation (1) for large ϵ might be an interesting model when the stationary pattern is determined locally on a single length scale without any relation to the cell boundaries.

C. Defect motion

The interaction of defects with each other and with lateral boundaries and the appearance and changes in height of barriers to defect motion (which has been discussed previously in the context of a stochastic model for the onset of turbulence[70]) can be studied by using controlled initial conditions similar to those first used by Chen and Whitehead[10] (Figs. 19–23). In the following, we briefly discuss some simple numerical experiments that illustrate defect climbing and gliding and the dependence of these motions on the reduced Rayleigh number. Further com-

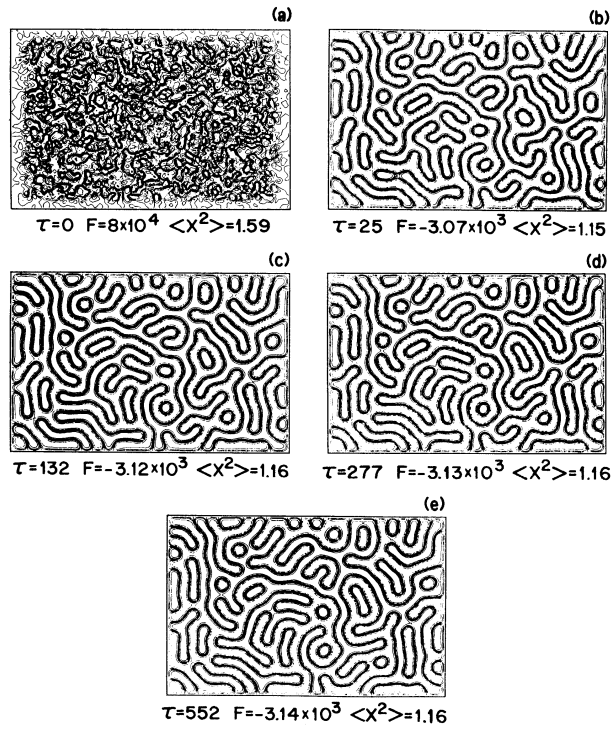

FIG. 18. Pattern evolution for $\epsilon=2.0$, using the identical initial conditions and parameters as Fig. 10. The evolution is even more rigid and slow than Fig. 16 and the boundaries play a minor role in determining the pattern orientation. In particular, the density of defects is constant and rolls are no longer normal to the boundaries.

parisons will be given later in the next section (Sec. V) with runs in cells with periodic boundary conditions.

Dislocation climbing is shown in Figs. 19 and 20. For laterally infinite cells, the two dislocations in Fig. 19(a) would climb away from each other at a constant velocity that is proportional to $\delta q^{3/2}$ (for $\epsilon \ll 1$), where $\delta q = q - q_0$ is the difference with the critical wave number and is a measure of the positive compression of the rolls driving the climbing motion.[21,22] In the presence of rigid lateral walls, Fig. 19 shows that the defects climb only a finite distance away from each other, stopping at first glance a length scale of $(\epsilon - \epsilon_c)^{-1/2}$ away from the lateral walls. Similar runs for different values of ϵ show that there is a barrier for all values of ϵ that prevents a dislocation from annihilating at the boundary even though this would lower the Lyapunov value. (It is not known if this barrier exists when the dislocation axis lies at a finite angle with the lateral wall.) Figure 20 shows that a similar barrier to defect annihilation exists for attracting dislocations. Although Fig. 20 shows severe distortions of the surrounding rolls as the defects climb towards each other, related simulations described in Sec. V show that the barrier to annihilate is an intrinsic property of the core region of the defect. The barrier is not related to the roll distortions induced by the boundaries.

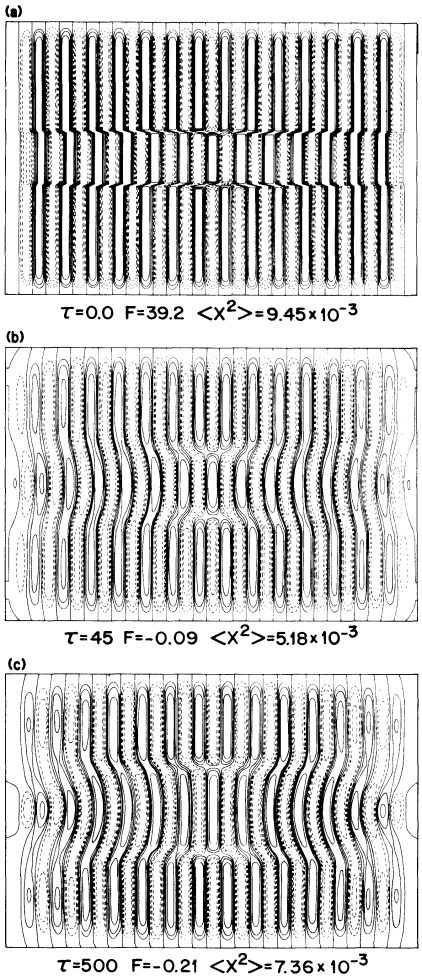

FIG. 19. Example of dislocation climbing in a large rectangular cell of aspect ratio $\Gamma_x = 29$, $\Gamma_y = 20$ with $\epsilon = 0.05$ and a mesh of 193×129 points. Initial conditions were $\phi(x, y, \tau=0) = \sqrt{\epsilon}\sin(x)$ for $5L_y/12 \le y \le 7L_y/12$, and $\phi(x, y, \tau=0) = \sqrt{\epsilon}\sin(\frac{31}{29}x)$ otherwise. The dislocations repel but climb only a small distance from each other before becoming stationary. Defect motion is accompanied by significant roll distortions far away.

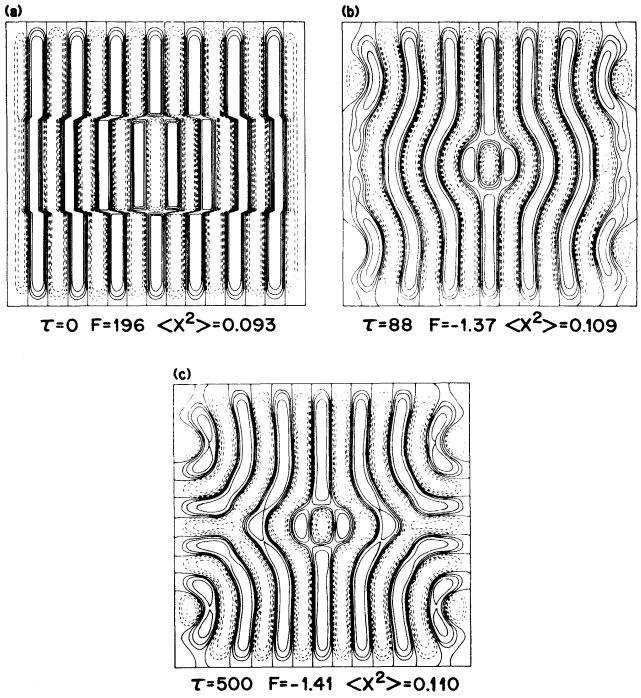

FIG. 20. Example of dislocation climbing in a large square cell of aspect ratio $\Gamma_x = \Gamma_y = 15$ with $\epsilon = 0.25$ and a mesh of 97×97 points. Initial conditions were $\phi(x, y, \tau=0) = -\sqrt{\epsilon}\sin(\frac{17}{15}x)$ for $L_y/3 \le y \le 2L_y/3$, and $\phi(x, y, \tau=0) = -\sqrt{\epsilon}\sin(x)$ otherwise. The defects now attract and climb towards each other. They do not annihilate for any value of ϵ starting from these initial conditions. As In Fig. 19, the defect motion is accompanied by severe roll distortions even far away from the core region. (c) is stationary. Distance of closest approach of the dislocations is independent of ϵ.

Examples of dislocation gliding are given in Figs. 21–23. The theory of gliding[22] is much weaker than that of climbing[21,22] and the quantitative rules relating the dislocation velocity to the shearing of the surrounding rolls driving the gliding have not yet been worked out. When the dislocations are parallel and close to the lateral walls (Fig. 21), they are attracted towards the walls, where they merge and annihilate [Fig. 21(e)]. If the dislocations have opposite sign and their separation is small compared to their distances from the lateral walls, they glide towards each other and eventually annihilate (Fig. 22). If the dislocations have the same signs, they glide away from each other but only a finite distance (Fig. 23), suggesting that their interaction is short ranged. Figure 23 shows that even in a large cell of aspect ratio 32 by 16, the defect motion is accompanied by distortions of rolls far away and by some climbing so that the resulting motion is diffi-

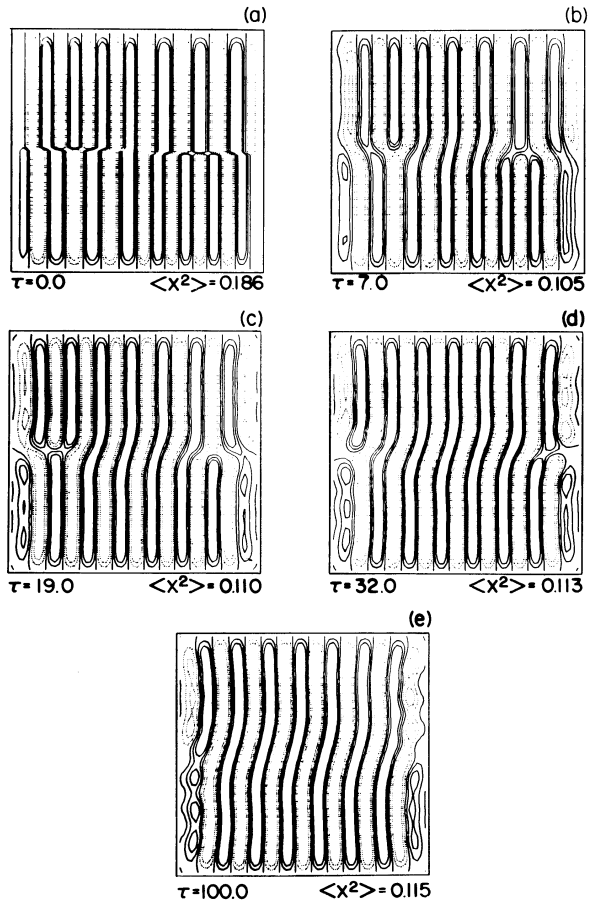

FIG. 21. Example of dislocation gliding in a square cell with $\Gamma_x=\Gamma_y=16$, $\epsilon=0.25$, and a 97×97 mesh. Initial conditions were $\phi(x,y,\tau=0)=\sqrt{\epsilon}\sin(\frac{14}{16}x)$ for $x\le L_x/2$ and $y\le L_y/2$, or $x\ge L_x/2$ and $y\ge L_y/2$, and $\phi(x,y,\tau=0)=\sqrt{\epsilon}\sin(\frac{18}{16}x)$ for $x\le L_x/2$ and $y>L_y/2$, or $x\ge L_x/2$ and $y<L_y/2$. The wave numbers $\frac{14}{16}$ and $\frac{18}{16}$ were chosen to be stable with respect to the Eckhaus instability; zigzags, do not appear. Dislocation on the left side glides left and eventually annihilates at the boundary; a similar behavior occurs on the right side. Meanwhile, some wave-number adjustment occurs at the upper-left and lower-right vertical sides, where a positive and negative roll disappears, respectively.

cult to analyze. Much more experimental and numerical work, studying especially the dependence of defect motion on Prandtl number, would be useful.

The velocity of dislocation gliding decreases as ϵ increases and ceases altogether for $\epsilon\gtrsim0.7$. Starting from the initial conditions of Fig. 22(a) with $\epsilon=0.90$, we found neither climbing nor gliding, although local adjustments of the rolls near the walls took place. Similar runs were studied with $\epsilon=0.90$ for Figs. 19 and 20 and did not show any noticeable decrease in the climbing velocity. This suggests that barriers to defect gliding but not climbing appear and grow in height as ϵ increases. This partially explains the rigidity of the disordered pattern formation observed in earlier sections, particularly in Figs. 16 and 18.

D. Long-time asymptotic behavior

An issue raised by the simulations discussed in this section, particularly by Fig. 12(d), is the long-time asymptotic behavior of the Nusselt number. (The long-time behavior of a phase sensitive quantity like the midpoint value of the field is not as interesting since the phase can vary arbitrarily even over long times and cannot be easily analyzed.) If the characteristic length scales were to relax immediately to $k_c=1$, the $(\Delta+1)^2$ term would vanish and Eq. (1) would reduce to the standard Ginzburg-Landau equation[2]

$$\partial_\tau\phi=\epsilon\phi-\phi^3 \tag{21}$$

or, equivalently,

$$\tfrac{1}{2}\partial_\tau\phi^2=\epsilon\phi^2-\phi^4 ,$$

where we can identify ϕ^2 with $\langle\phi^2\rangle$ since the spatial modes are assumed frozen. Then it is well known[2] that ϕ^2 relaxes *exponentially* to its stationary state as

$$\phi^2(\tau)-\phi^2(\tau=\infty)\simeq\exp(-2\epsilon\tau)\ \text{ as }\ \tau\to\infty\ . \tag{22}$$

If, on the other hand, ϕ^2 is roughly constant, we can absorb it into ϵ and ignore the nonlinear term to obtain a biharmonic diffusion equation (in an infinite cell),

$$\partial_\tau\phi=[\epsilon-(\Delta+1)^2]\phi\ . \tag{23}$$

A simple application of Laplace's method[71] shows that ϕ decays asymptotically as a power law ($\tau^{-1/2}$) in any dimension. Thus in these two limits, we get exponential or power law behavior (ignoring the boundaries and defect motion). The numerical simulations show that $\langle\phi^2\rangle$ generally approaches its limiting value *exponentially* except in large cells where a linear power law seems to occur [Fig. 12(d)]; the power is not easily extracted because of the few significant digits (three in nearly all simulations). In Fig. 12(d), $\langle\phi^2\rangle$ relaxes almost linearly towards its stationary value. The time dependence of the evolution in Fig. 19 is shown on a semilogarithmic scale in Fig. 24 and is clearly exponential over most of the evolution. This is so even though the spatial degrees of freedom are evolving so that Eq. (21) is not correct. The decay constant extracted from Fig. 24, 0.02, is comparable in magnitude with the value of 2ϵ predicted by Eq. (22). Repeated runs using identical initial conditions and values of ϵ ranging from 0.05 to 0.55 in steps of 0.1 show no simple scaling behavior of the decay constant (obtained by least-squares fits) with ϵ. Instead, the decay is roughly constant with a value near 0.05. The exponential tail is currently not understood. It would be interesting for experimentalists to pursue this question in large and small cells to examine the possibly simple asymptotic behavior in the heat flux near onset.

V. PATTERN FORMATION AND DEFECT MOTION: PERIODIC BOUNDARY CONDITIONS

The effect of lateral boundaries on pattern formation can be further illuminated by repeating several of the numerical experiments of the previous section with periodic boundary conditions, Eq. (3b). This eliminates the pres-

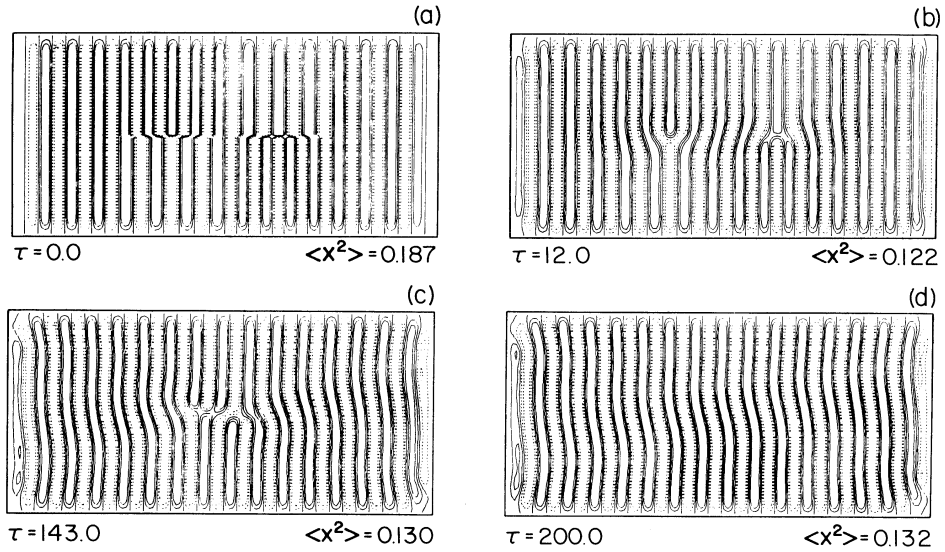

FIG. 22. Example of dislocation gliding in a large rectangular cell with $\Gamma_x=32$, $\Gamma_y=16$, $\epsilon=0.25$, and a 129×97 mesh. Initial conditions were those of Fig. 21 embedded in the middle of the present cell, with rolls of the critical wave number on both sides. The dislocations, which are now closer to each other than to the sidewalls, attract, glide, and annihilate leaving the almost stationary state in (d). Here, as in Fig. 21, ϵ is just large enough to prevent significant cross-roll formation at the sidewalls.

ence of rigid walls and corners while still preserving the relaxational and ordering properties of the Lyapunov functional, Eq. (4). [This does not mean that evolution in a finite cell with periodic boundary conditions is equivalent to evolution in a finite region of an infinite-aspect ratio cell. Infinitesimal rotations or translations will generally not be consistent with Eq. (3b)]. Although periodic boundary conditions cannot be studied in the laboratory, our conclusions about the time scale needed to become stationary should still hold if the "soft" boundary conditions of L. Kramer *et al.*[30] were to be imposed on all four sides of a large cell. These boundary conditions would greatly reduce the pinning tendency of the corners.

Figure 25 illustrates pattern formation with periodic boundary conditions in small- and medium-aspect-ratio cells and should be compared to Figs. 5, 6, and 7. Al-

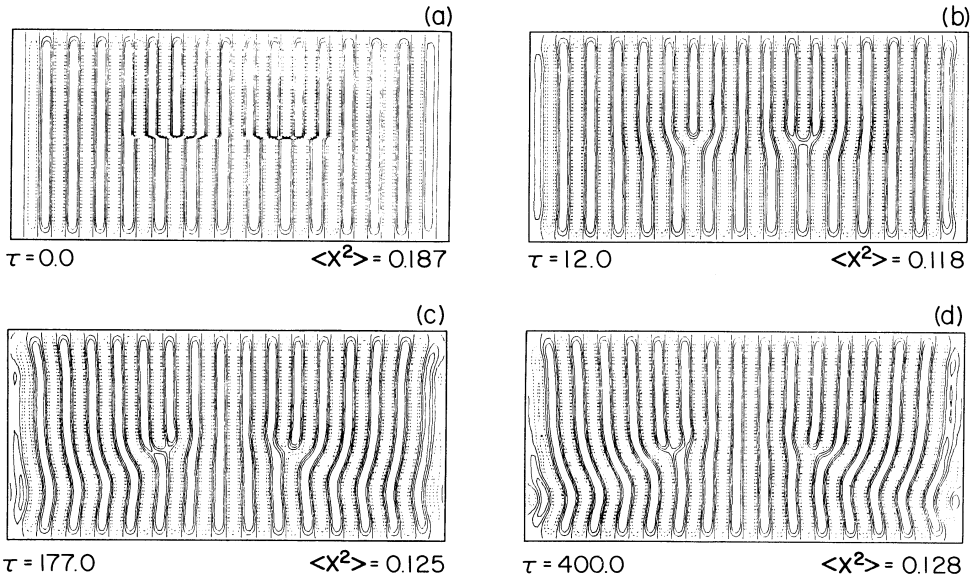

FIG. 23. Example of dislocation gliding between dislocations of the same sign; the interaction is now repulsive. Here $\Gamma_x=32$, $\Gamma_y=16$, $\epsilon=0.25$, and a 129×97 mesh was used. Initial conditions were $\phi(x, y, \tau=0)=\sqrt{\epsilon}\sin(\frac{14}{16}x)$ for $x\geq L_x/4$, and $x\leq 3L_x/4$ and $y\leq L_y/2$; $\phi(x, y, \tau=0)=\sqrt{\epsilon}\sin(\frac{18}{16}x)$ for $x\geq L_x/4$, and $x\leq 3L_x/4$ and $y>L_y/2$; and $\phi(x, y, \tau=0)=\sin(x)$ otherwise. The dislocations glide a short distance away from each other, suggesting that their interaction is short ranged. The defects also climb a small amount and rolls far away at the boundaries become significantly distorted.

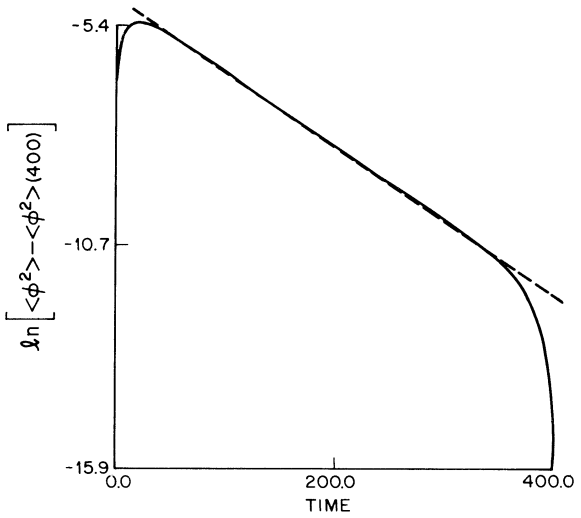

FIG. 24. Time dependence of the mean-square amplitude $\langle \phi^2(x,y,\tau) \rangle$ for the dislocation climbing of Fig. 19, plotted on a log-linear scale, $\langle \phi^2(400) \rangle$ is the last time point of the series at $\tau=400$. Dotted line was obtained from a least-squares fit over the range $50 \leq \tau \leq 350$ and yielded a slope of -0.02, roughly of order ϵ. Time dependence is exponential except for the short intervals at the beginning and at the end.

though the intermediate stages of the evolution [Figs. 25(b) and 25(c)] are similar to the intermediate stages of Fig. 5, the time scale to become stationary is considerably smaller. There is no tendency for the rolls to become parallel to the shorter sides. Repeated integrations with different random initial conditions show that the degeneracy of stationary solutions is much larger than that of Fig. 5 but in a trivial way since the other solutions differ only in orientation and not in texture. [The degeneracy is finite because of Eq. (3b)].

An interesting feature of the evolution in Fig. 25 is that there are no defects in the stationary solution even though $\epsilon > 1$. In contrast, for rigid boundary conditions and for the same aspect ratio and value of ϵ, random initial conditions were found to yield disordered textures that do *not* anneal out to become straight rolls parallel to the shorter side. (Thus defects survive when $\epsilon \gtrsim 1$ even for cells whose rigid lateral boundaries are close to each other.) This result does not contradict our earlier observation that barriers to defect motion prevent significant pattern evolution when ϵ is large. Periodic boundary conditions so severely restrict the evolution in *small* cells (for example, a defect in a boundary cannot glide an infinitesimal amount) that nearly all initial conditions are close to a stationary state of lower Lyapunov value consisting of parallel rolls. For large cells (not shown), the periodic boundary conditions are less restricting and most random initial conditions for large ϵ do indeed lead to states similar to Figs. 16 and 18.

An example of pattern formation in large cells is given in Fig. 26 which should be compared with Fig. 15. For periodic boundary conditions and near onset, all defects eventually disappear, leaving straight or wavy parallel rolls [Fig. 26(e)]. This confirms directly that defects are the result of a competition between bulk effects forcing the rolls to be parallel, and rigid boundaries forcing the rolls to be normal to the side walls.[8] In Fig. 26, the random initial conditions simplify to give two dislocations [Fig. 27(c), but more easily studied in Fig. 27] which glide towards each other and annihilate. The resulting pattern has a smaller local wave number than k_c and is unstable to the zigzag instability (see Sec. VI) which gives the wig-

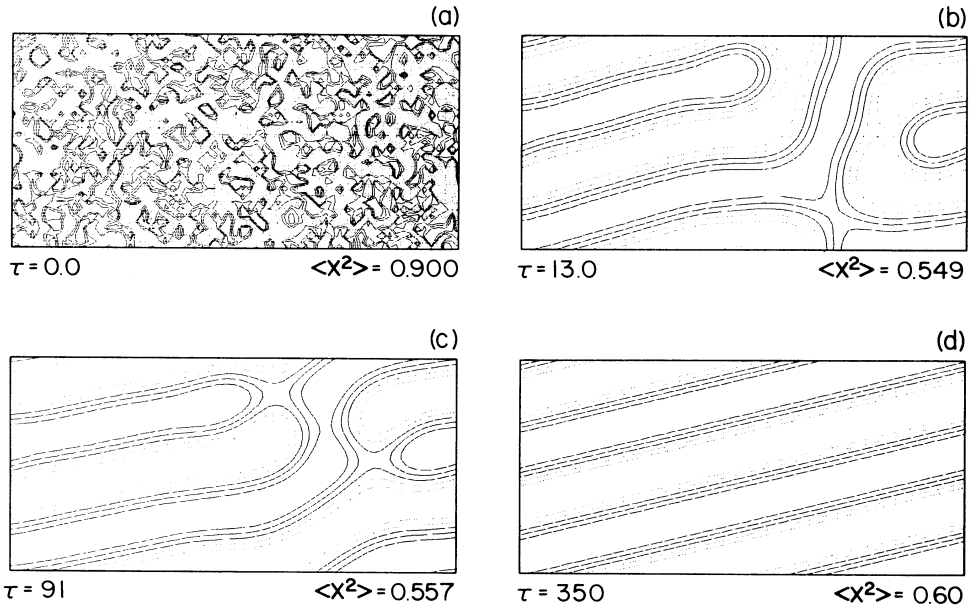

FIG. 25. Pattern formation with periodic boundary conditions for a small rectangular cell. Here $\Gamma_x=8$, $\Gamma_y=4$, $\epsilon=1.50$, and a 64×64 mesh was used. Unlike Fig 5, the rolls no longer have any tendency to orient parallel to the shorter side. Although $\epsilon > 1$, the strong constraints imposed by the periodic boundary conditions make all initial conditions close to a stationary state of parallel rolls and all defects anneal out (compare Figs. 16 and 18).

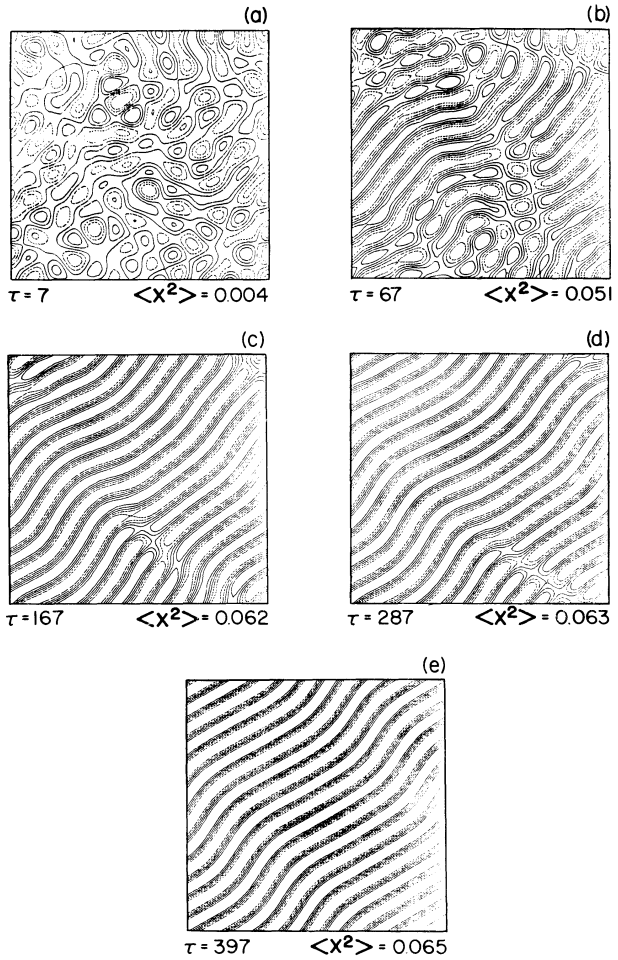

FIG. 26. Pattern formation with periodic boundary conditions for a large square cell; $\Gamma_x = \Gamma_y = 16$, $\epsilon = 0.10$, and a 96×96 mesh was used. The random initial conditions simplify on a short-time scale ($\lesssim \tau_h$) to two attracting dislocations in (c). (This is more easily seen in Fig. 27.) The dislocations glide towards each other in (d), annihilate, and leave a defect-free texture of wavy rolls in (e), which is stationary. Other runs close to onset in large cells show a similar evolution (not shown): all defects disappear leaving straight or wavy rolls of random orientation. The time to become stationary is about one horizontal diffusion time, unlike Fig. 15.

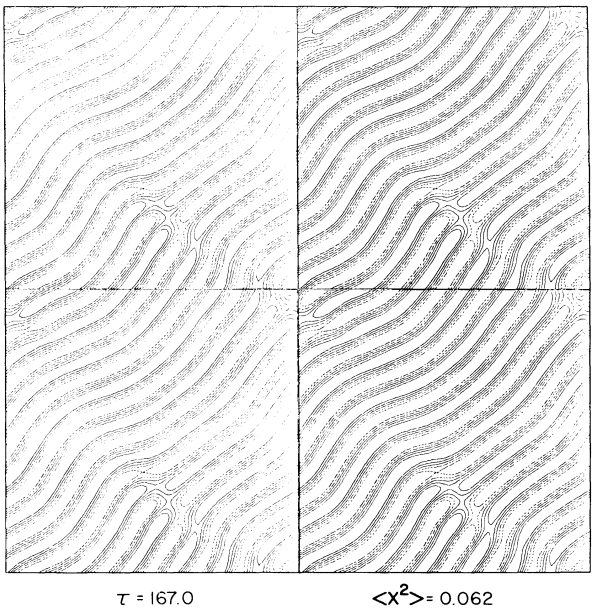

FIG. 27. The two dislocations of Fig. 26(c), shown in greater detail. This figure is made from four unit cells and shows more clearly the way that the rolls and defects extend across the periodic boundaries.

gly stationary state of Fig. 26(e). This state cannot adjust its wave number closer to k_c by eliminating the wiggles since this would require small motions that are inconsistent with the periodic boundary conditions. Other random initial conditions give straight or wavy parallel rolls of different orientation. Eliminating the rigid boundaries increases the degeneracy of the nonlinear stationary solutions but in a trivial way.

A striking feature of Fig. 26 is that the time to become stationary is now about a horizontal diffusion time and is much less than the corresponding time in Fig. 15. This suggests that the long-time scale to become stationary in Fig. 15 arises from the competition between bulk and boundary effects and *not* from the complicated dynamics of interacting defects.[26] Indeed the short-time scales of Figs. 16 and 18 suggest the stronger conclusion that the long-time scale arises only when there are two distinct length scales present, $2\pi/k_c$ and the much larger healing length of order $(\epsilon - \epsilon_c)^{-1/2}$.

Periodic boundary conditions are also helpful in further understanding the climbing defect motion of Figs. 19 and 20. Figure 28 shows the large ϵ evolution starting from the same initial conditions as Fig. 19(a) (the small ϵ evolution is almost identical). The dislocations climb only a short distance from each other and stop; this distance is the same in Figs. 19 and 28. Also, in both cases, the two dislocations are closer to each other in the stationary state than to their mirror images. We conclude that the distance separating the dislocations is not determined by the size of the healing length, by the interactions of the defects with their images, or by the distortions of surrounding rolls as they adjust to the rigid boundaries. Instead, the distance must be determined by a balance between their repulsive and attractive interactions.[21] These depend on the two wave numbers and the size of the box.

The case when dislocations climb toward each other, corresponding to Fig. 20, are given for small and large ϵ in Figs. 29 and 30, respectively. [The initial conditions were the same in both cases, Fig. 20(a)]. Figure 29 shows that the evolution close to onset of attracting dislocations is more complicated for periodic boundary conditions. As the dislocations climb towards each other [Figs. 29(a) and 29(b)], the compression and resulting curvature of the rolls excite cross rolls. These grow to give a stationary pattern of primarily rectangular convection cells [Fig. 29(c)]; the original pair of defects can no longer be defined. Other simulations of defect pairs close to onset, for example, two pairs of dislocations (not shown), yield stationary states of *uniform* rectangular convection cells.

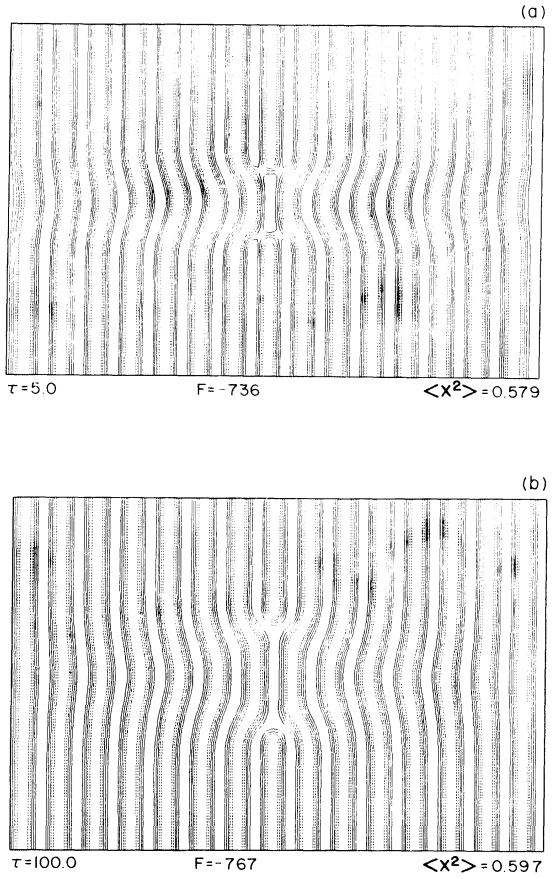

FIG. 28. Defect climbing *not* near onset for repulsive dislocations and with periodic boundary conditions. Initial conditions and aspect ratio are the same as for Fig. 19 except $\epsilon=0.90$. Velocity of climb and the separation of the dislocations in the stationary state (b) are the same as for Fig. 19 and for smaller ϵ. This suggests that the distance of separation is not due to the interaction with mirror images, to the presence of lateral walls, or to the value of the reduced Rayleigh number.

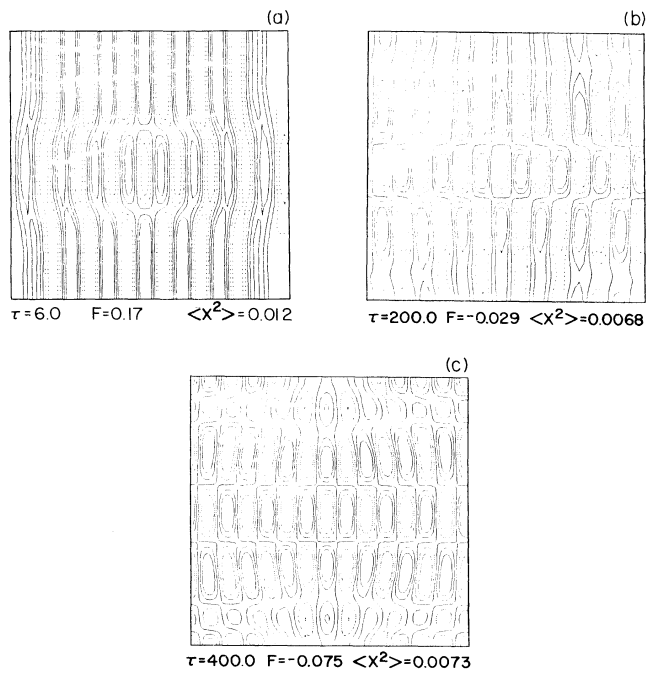

FIG. 29. Defect climbing near onset for attractive dislocations and with periodic boundary conditions. Aspect ratio and initial conditions are the same as for Fig. 20; here $\epsilon=0.025$ and a 64×64 mesh was used. As the dislocations move closer to each other (b), cross rolls are excited. These grow and evolve to give a superposition of rolls near the center of the cell, a rectangular texture of alternating positive and negative domains. Original pair of defects can no longer be identified in the stationary state (c).

The stability of these textures is difficult to understand. Although stationary nonlinear rectangular solutions exist over a significant range of wave numbers k_x and k_y for Eq. (1) with boundary conditions Eq. (3b), a stability analysis shows that all such solutions are unstable.[67] (Frick, Busse, and Clever also have found that unstable stationary rectangular solutions exist for the Boussinesq equations in the limit of large Prandtl number.[72]) In particular, these solutions are everywhere unstable to perturbations that are periodic in k_x and k_y, suggesting that the rectangular texture will evolve to become locally single parallel rolls. One explanation for the appearance of rectangular textures in the stationary state, Fig. 31(c), is that the vertical reflection symmetry of the initial conditions is preserved during evolution. Thus perturbations do not appear that can break the symmetry, favoring one of the possible orientations of parallel rolls. It is interesting that the rectangular unit cell in Fig. 29(c) is such that $k_x^2+k_y^2\simeq1$ although both k_x and k_y are not close to the critical wave number. The cross rolls appear [Fig. 29(b)] with just the right wave number to give a wave vector whose magnitude is close to k_c. Rigid boundary conditions prevent cross roll formation in large cells [see however Fig. 7(d) and Fig. 8(a)]; rectangular textures have not been seen, numerically or experimentally, close to onset.

For larger ϵ, the rectangular cells do not form [Figs. 30(a) and 30(b)]. The dislocations climb towards each other and fail to annihilate. By comparing Fig. 30(b) with Fig. 20(c), we see that the separation of the defects in the stationary state and the barrier to annihilate is an intrinsic property of the core region of the defects and is not a result of the severe distortions of the surrounding rolls [Fig. 20(c)].

Similar experiments can be made for defect gliding although the initial conditions in Figs. 21(a), 22(a), and 23(a) must be modified since they are not periodic in the vertical direction. Suitable initial conditions are easily constructed by going to cells of twice the height and using the initial conditions of Figs. 21—23 together with their images through the horizontal midline of the larger cells. The resulting evolution (not shown) is similar to that already described. The only difference is for Fig. 21, where the dislocations no longer glide, being equidistant from themselves and their mirror images.

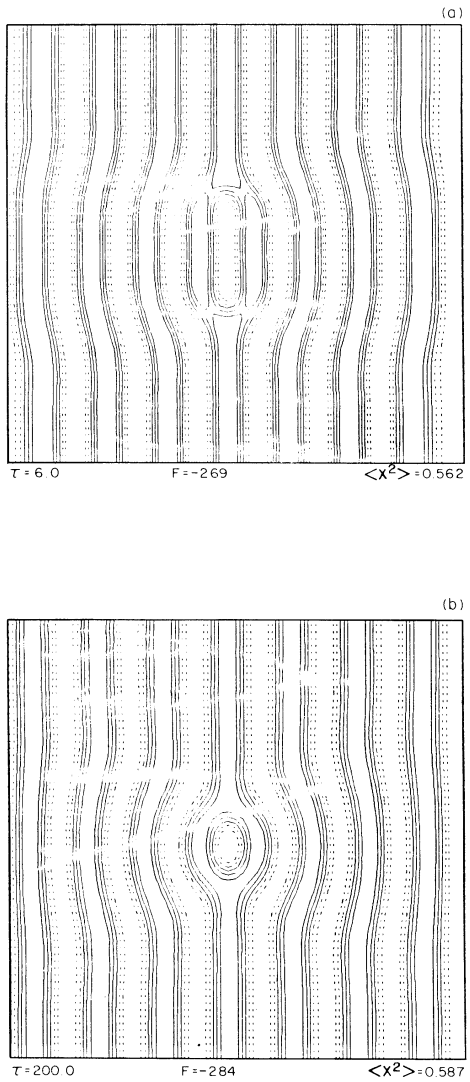

FIG. 30. Defect climbing not near onset for attracting dislocations and with periodic boundary conditions. All parameters are the same as for Fig. 29 except ϵ was set to 0.90. Distance of closest approach is the same as for Fig. 20, suggesting that this distance is determined intrinsically by the core region and not by distortions of surrounding rolls or by the value of ϵ.

VI. GROWTH AND SATURATION OF LINEAR INSTABILITIES IN THE PRESENCE OF BOUNDARIES

Busse and collaborators[4,20] have shown that the time dependence and wave-number selection in Rayleigh-Bénard experiments can be usefully and even semiquantitatively understood by a linear stability analysis of stationary nonlinear parallel-roll solutions in an infinite cell. The physical reason is that the fluid exists as two-dimensional rolls even for large Rayleigh numbers[28] and the various instabilities simply shift the wave length without significantly changing the local roll structure. In this section, we look at the linear stability boundaries of Eq. (1) and at the evolution and saturation of the various instabilities. In this way, the effect of finite boundaries and nonlinear terms can be studied and related to experiment.

In Fig. 31, we show the stability boundaries of Eq. (1) as a function of ϵ and the stationary nonlinear roll wave number, K. This figure was obtained by a Galerkin method similar to that of Clever and Busse;[73] the present case is much simpler since the z dependence has been removed from the equations. First, solutions of the form

$$\phi_0(x,y)=\sum_{n=1}^{N} a_m \sin[(2n+1)Kx] \tag{24}$$

are found that satisfy Eq. (1) (only odd harmonics are needed because of the cubic nonlinearity and only a few terms, $N \lesssim 3$, are needed for good convergence[67]). The stability of ϕ_0 with respect to an infinitesimal perturbation, $\delta\phi(x,y,\tau)$, is then studied by solving the linear eigenvalue problem

$$[\epsilon-(1+\Delta)^2-3\phi_0^2]\delta\phi=\lambda\,\delta\phi \tag{25}$$

for the growth rate λ [which can only be real since Eq. (1) is first order in time]. Because Eq. (25) has a periodic operator with period K, one can use Floquet theory[71] (alternatively, Bloch's theorem[74]) to write $\delta\phi$ as a plane wave times a function periodic in x

$$\delta\phi(x,y,\tau)=\exp[\lambda\tau+i(k_x^*x+k_y^*y)]\sum_{m=-N}^{N} d_m \sin(mKx)\,,$$

where (k_x^*,k_y^*) is the wave vector of the perturbation. For a given ϵ and wave number K, the maximum value of λ in Eq. (25) is determined by varying k_y^* over all positive numbers and k_x^* over the irreducible part of the Brillouin zone,[74] $[0,K/2]$. The band of stable wave numbers and specific instabilities are found by varying K for fixed ϵ to find the zeros of the maximum eigenvalue λ. Unlike the Boussinesq equations,[4,20] there are no oscillatory, skewed-

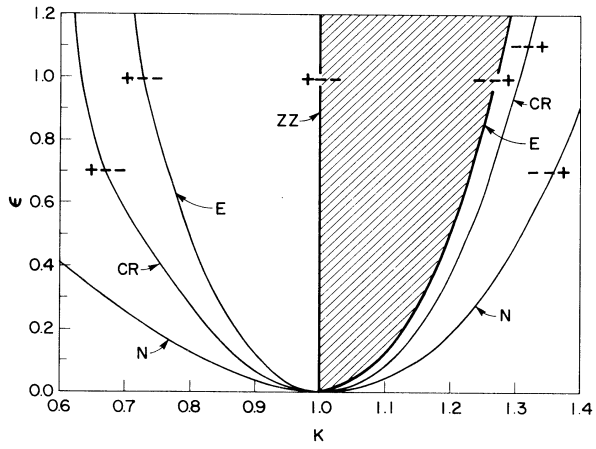

FIG. 31. Linear stability analysis of Eq. (1) for stationary parallel nonlinear rolls of wave number K. Stability region (shaded) lies between the zigzag branch at $K=1.0$ and the Eckhaus branch for $K>1.0$. Oscillatory, knot, and skewed-varicose instabilities do not occur for Eq. (1). Stability boundaries for the Eckhaus and cross-roll instabilities are in remarkably good agreement with the small-ϵ analytical expression, even for ϵ of order 1.

varicose, or knot instabilities. The properties of the cross-roll, Eckhaus, and zigzag instabilities that do occur in Eq. (1) are summarized in Table I. More details and the stability boundaries of two-dimensional equations that include the generation of vertical vorticity with mean drift will be given elsewhere.[67]

It is interesting to compare Fig. 31 with the small-ϵ analytical expressions for the stability boundaries and with the corresponding stability diagram of the Boussinesq equations in the limit of large Prandtl numbers.[75,76] For Eq. (1), both the cross-roll and Eckhaus instabilities are known analytically for small ϵ. They are as follows:

$$\epsilon = 12(K-1)^2, \quad \text{Eckhaus}$$

$$\epsilon = 8(K-1)^2, \quad \text{cross roll} .$$

These expressions turn out to be accurate for our model even for $\epsilon \gtrsim 1.0$, as we see from Fig. 31. The reason is that the operator $(\Delta+1)^2$ forces the nth harmonic in Eq. (24) to be damped as n^{-4} so a single mode is a good approximation even for $\epsilon \simeq 1$. The cross-roll and Eckhaus instabilities reverse roles as the most dangerous instability bounding the band of stable wave numbers in going from the $\sigma = \infty$ Boussinesq amplitude equation to Eq. (1). [This difference derives from our constant approximation for the coupling function g in Eq. (5); it does not lead to any qualitative changes in the spatial evolution.] The stability region of the Boussinesq equations in the limit of infinite Prandtl number[75,76] is bounded and a wave number stable at small ϵ must become unstable for large enough ϵ. Equation (1) does not have this property and a wave number stable for a given value of ϵ will remain stable for large ϵ, leading to only trivial wave-number selection. The stability boundaries of Eq. (1) are not as interesting as those of the Boussinesq equations.

The instability of rolls in numerical simulations are difficult to compare with real experiments since the simulations are free of fluctuations to a greater degree than in any experiment. For example unstable parallel rolls in a cell with periodic boundary conditions are found not to evolve since there are no perturbations to grow (either induced or created by the presence of corners). In Figs. 32, 34, and 35, we study the instability of unstable rolls arising solely from perturbations diffusing in from the rigid boundaries. In Figs. 33 and 36, we add external perturbations to start the desired instability.

The simplest example to study of the effect of lateral boundaries on instabilities is for rolls that lie outside the neutral stability curve, N, separating stable conduction ($\phi = 0$) from convection solutions. Figure 32 shows how

TABLE I. Description of linear instabilities of Eq. (1).

Type	Properties
Cross roll	Short-wavelength instability with $k_x^* = 0$, $k_y^* = O(1)$
Eckhaus	Long-wavelength instability with $0 < k_x^* \ll 1$ and $k_y^* = 0$
Zigzag	Long-wavelength instability with $k_x^* = 0$, $0 < k_y^* \ll 1$

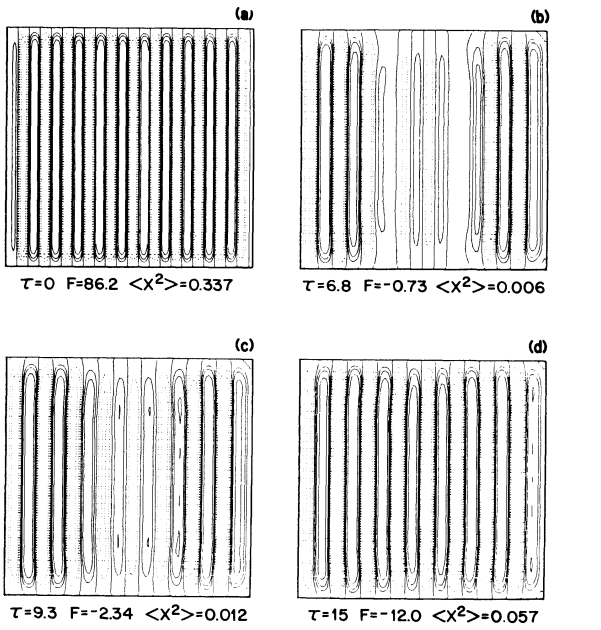

FIG. 32. Evolution of parallel rolls lying outside the neutral stability boundary (see Fig. 31) in a cell of aspect ratio $\Gamma_x = \Gamma_y = 16$, with $\epsilon = 0.25$ and a 97×97 mesh. Initial wave number was $K = 1.40$. Decrease in amplitude is not uniform and is most rapid near the center of the cell.

rolls of wave number $K = 1.4$ evolve. In the absence of walls or for periodic boundary conditions, the amplitude of the rolls would decay *uniformly* to zero[77] while small perturbations would slowly grow up in amplitude to give wave numbers inside the stability region, $1 \lesssim K \lesssim 1.14$. We see that the amplitude does decrease everywhere but much more rapidly in the interior of the cell. The rolls near the sidewalls decrease in magnitude and simultaneously swell to a larger wavelength. In the meantime residuals of the interior rolls grow back up in magnitude [Fig. 32(b)] and join up with the rolls near the boundaries, yielding a pattern at the critical wavelength [Fig. 32(d)], which gives the smallest Lyapunov functional for parallel rolls in this size cell.

The evolution of the cross-roll instability is given in Fig. 33. We have imposed a small perturbation of cross rolls in Fig. 33(a) (at the critical wave number) to start cross-roll formation,

$$\phi_0(x,y) = \sqrt{\epsilon}[\cos(Kx) + \alpha \cos(y)] .$$

The resulting evolution depends sensitively on α. For $\alpha \lesssim 0.05$, the cross-roll perturbation dies out and the rolls expand, squeezing out rolls at the boundaries. For $\alpha \gtrsim 0.20$, the perturbation grows in rapidly and the underlying roll pattern decays, yielding parallel rolls at the critical wavelength perpendicular to the orientation of the initial conditions. This is often observed in both small[10]- and large[76]-aspect ratio experiments with controlled initial conditions. For $\alpha \simeq 0.15$, we get the evolution of Fig. 33. The length scale in the center of the cell is shifted towards the critical wave number by two generations of cross rolls, the first leading to cross rolls perpendicular to the original

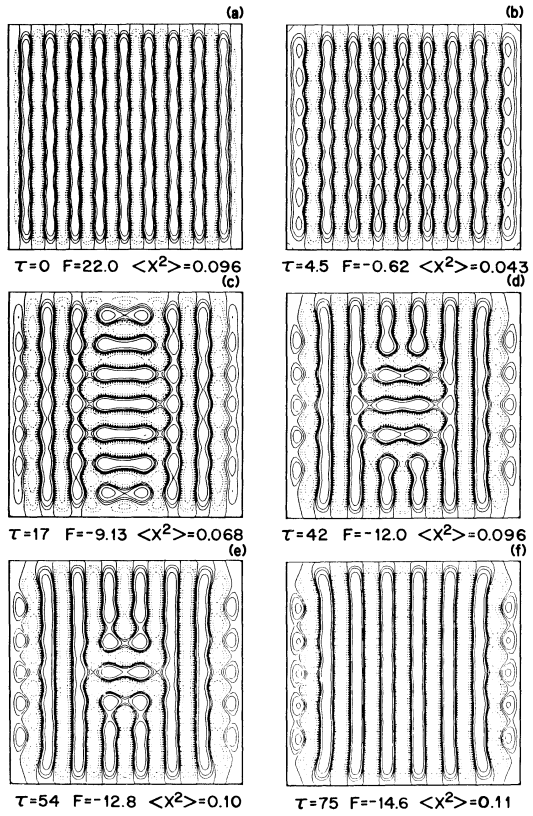

FIG. 33. Cross-roll instability in a large square cell of aspect ratio $\Gamma_x=\Gamma_y=15$, with $\epsilon=0.25$ and a 97×97 mesh. Initial condition was $\phi=\sqrt{\epsilon}\{\cos[1.25(x-L_x/2)]+0.15\cos(y-L_y/2)\}$; the small y-dependent cross roll was added to start the instability. Resulting pattern depends on the amplitude of this perturbation. The value 0.15 is close to the critical value at which the underlying cross rolls of wave number 1.25 decay, leaving orthogonal rolls only.

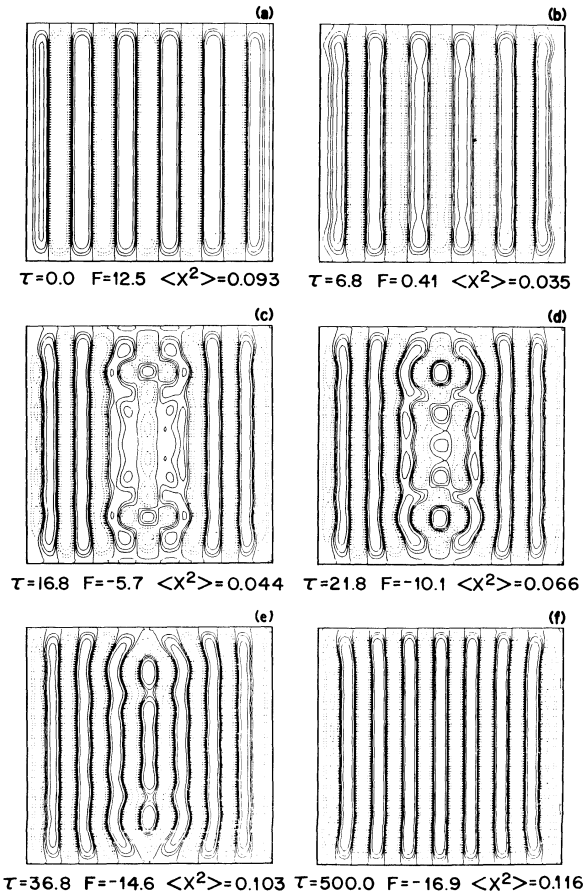

FIG. 34. Example of the zigzag instability in a large square cell of aspect ratio $\Gamma_x=\Gamma_y=16$, with $\epsilon=0.25$ and a 97×97 mesh. Initial wave number in (a), $K=0.70$, is unstable to Eckhaus, cross-roll, and zigzag instabilities. Once deviations in the x direction occur, as in (c), the cross roll can grow. (d) and (c) probably involve both zigzag and cross-roll instabilities.

orientation [Figs. 33(b) and 33(c)] and the second generation forming cross rolls on top of these. This second generation of rolls arises from the already discussed instability of rolls parallel to the sides [see Fig. 9 and Fig. 33(c)]. We see from Fig. 33 that the growth rate of cross rolls is also damped near the boundaries. The length scale over which the growth rate is depressed is significantly larger than the healing length of the convection amplitude, which is only one roll pair for Fig. 33.

The perturbation arising from the presence of rigid sidewalls does not excite zigzag-like instabilities unless the wave number is unstable to both zigzags and cross rolls; for wave numbers unstable only to zigzag, the wave number is adjusted by rolls growing in from the boundaries, a one-dimensional mechanism. Figure 34 shows how the wave number is altered near onset for rolls of wave number $K=0.70$. Two new rolls are created in the center of the cell by a complicated evolution that is not simply zig zag or cross roll. The stationary state [Fig. 34(f)] has 16 rolls. For larger ϵ, the evolution is more readily interpreted as zigzags (Fig. 35) and seems qualitatively similar to the large Prandtl number instability observed experimentally by Busse and Whitehead,[76] who also used an initial wave number unstable to both zigzags and cross rolls. In both cases the growing instability on adjacent rolls overlaps, leading to a disordered texture.

It is interesting to observe that in Fig. 35 and Fig. 8 of Busse and Whitehead,[65] the instability is not really a long-wavelength instability since the wave number in the y direction varies from 0.5 to 0.7. This suggests that the growing modulation is partially due to the short-wavelength cross-roll instability. This hypothesis can be tested by adding a weak perturbation of random noise to rolls with a wave number that is unstable only to zigzags (Fig. 36). The resulting instability now has a wave number of 0.25 and resulting zigzags do not overlap in the nonlinear stationary solution [Fig. 36(c)]. It would be useful to repeat Busse and Whitehead's experiment with a wave number unstable only to zigzags to see how this long-wavelength instability manifests itself.

We do not present any figures for the Eckhaus instability. If perturbations are not imposed on cells of aspect ratio smaller than 30, we found that the wave number of rolls unstable to Eckhaus changed by rolls appearing or disappearing at the boundaries. This mechanism is simi-

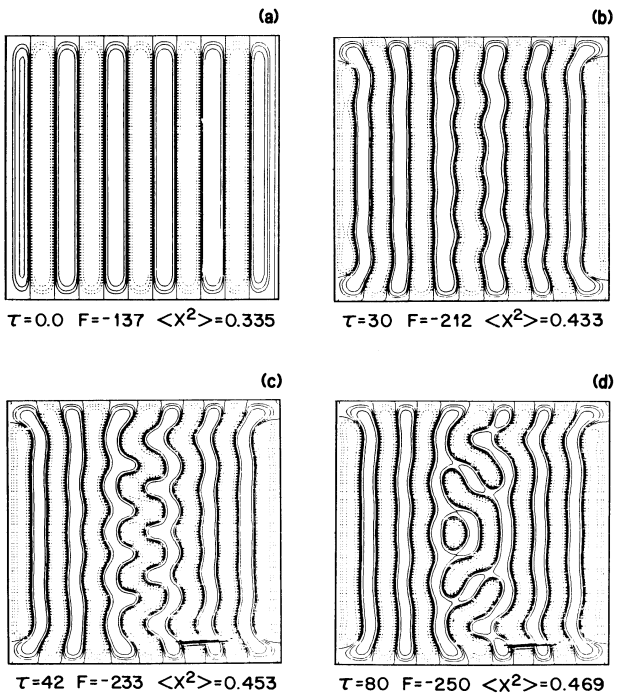

FIG. 35. Example of the zigzag instability for $\epsilon=0.90$, otherwise identical to Fig. 34. Zigzags are more evident and grow until they overlap, creating defects in the stationary state (d). The instability grows most rapidly away from the boundaries. While the zigzags are growing, new rolls appear from the vertical sides, (b), which is a sign perhaps of the Eckhaus instability.

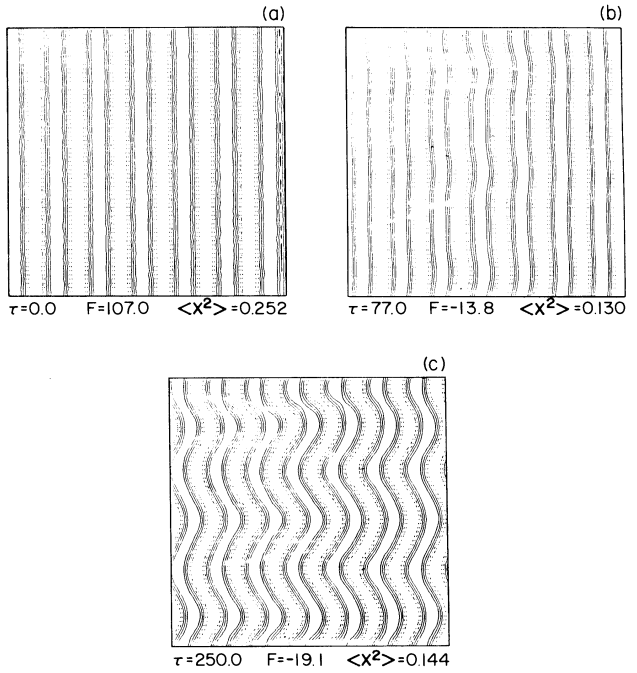

FIG. 36. Example of the growth and saturation of the zigzag instability for rolls with an initial wave number of $K=\frac{13}{16}$, which is unstable only to Eckhaus and zigzag instabilities. Periodic boundary conditions are used; $\Gamma_x=\Gamma_y=16$, $\epsilon=0.25$, and a 64×64 mesh was employed. A random field of mean-square value $0.05\sqrt{\epsilon}$ was imposed to start the instability (a). Growth and saturation in (b) and (c) occur with y wave numbers much smaller than that observed in Fig. 35; the zigzags do not overlap to create a disordered texture. This suggests that the short-wavelength cross-roll instability participates in the evolutions of Figs. 34 and 35.

lar to the one proposed by Cross and collaborators.[33,34] Bulk wave-number selection by Eckhaus might be observed by going to larger cells and by imposing random or sideband modes to start the instability. The time scale for adjustments to the wave number at the boundaries to diffuse in to the center of the cell would then be smaller than the time for bulk wave-number selection.

Several conclusions can be drawn from Figs. 31–36 and our earlier simulations. First, the linear stability analysis, Fig. 31, is only of limited use in understanding pattern formation in large cells near onset. The various instabilities act on short-time scales compared with defect motion over the cell. The defects therefore link domains of wave numbers that lie inside the stable region. The resulting evolution attempts to minimize the Lyapunov functional, Eq. (4). In contrast, for the Boussinesq equations (in medium Prandtl number fluids), the long-wavelength skewed-varicose instability pinches off rolls and eliminates or creates defects on a time scale comparable with defect motion.[19] The experimental pattern is generally too disordered[28] to determine whether the mean *local* wave number evolves to become stable. If the new wave number created by the skewed-varicose instability is also unstable, this would explain the appearance of turbulence at the same Rayleigh numbers for which this instability occurs.[19] Second, the above simulations suggest that no new instabilities occur for curved rolls and that the linear instability of *parallel* rolls suffices to understand the early stages in nonlinear evolution. This might not be the case when the generation of vertical vorticity is included at higher order in ϵ.[45,46,47] Third, we have seen that the growth rates of the various instabilities are suppressed or slowed down near boundaries. An exception is cross-roll formation in boundary layers (Fig. 9 and Ref. 35) which is nucleated by the presence of corners. Fourth, typically several wave number adjustment mechanisms occur simultaneously, e.g., the zigzag and cross roll in Fig. 34. Wave-number selection is likely to be a combination of bulk and boundary effects. Finally, the instabilities do *not* always lead to patterns of the critical wave number or to globally stable states. For large cells, the wave-number adjustment minimizes the Lyapunov functional *locally* which rarely leads to a global minimum.

VII. PATTERN FORMATION AND WAVE-NUMBER SELECTION IN FOURIER SPACE

For several reasons, it is fruitful to reexamine the various large cell simulations of the previous sections by following the changes of the spatial modes in wave vector or Fourier space.[28] First, Fourier analysis provides a way of analyzing the wave-number distribution for rigid boundaries and strongly disordered patterns. Most experiments and theories to date have emphasized one-

dimensional wave-number selection for which corners and defects can be ignored. Second, the issue of what mechanisms populate and select among the continuous band of stable wave numbers (Fig. 31) is not yet resolved although certain one-dimensional mechanisms have been suggested.[30–34] The following numerical results near onset show that a finite subband of stable wave numbers survive, centered close to the critical wave number. Finally there are some unambiguous trends in the experimental Fourier-space evolution[28] which we compare with our numerical results.

There are different possible selection mechanisms depending on the initial conditions. In the following, we emphasize the random initial-value problem in which length scales of all sizes with random wave vectors appear *with comparable magnitude.* As we mentioned in the Introduction, several numerical tests demonstrate for Eq. (1) that the details of the pattern formation are not sensitive to the average magnitude of the initial conditions but only to the orientation and magnitude of the wave vectors initially present. Although the final state does depend on the rate at which ϵ is ramped from below ϵ_c to just above,[9] we shall explore only the experimental case of an instantaneous change in ϵ. Some theory exists for this random initial-value problem in one dimension,[78] showing that the entire band of stable wave numbers bounded by the Eckhaus instability[79] will survive if this band is uniformly populated initially. Our results for two dimensions show that this is too lenient and only wave numbers close to the critical wave number survive. This is expected since the Lyapunov functions, Eq. (4), especially favors these wave numbers. For unrelated reasons, these are also the most rapidly growing modes[23,78] and an unambiguous statement about the origin of the selection principle is difficult.

One disadvantage of the Fourier method for Eq. (1) is that the resolution in wave number caused by the finite boundaries is comparable with the size of the stable band of wave numbers near onset. Unambiguous selection can be measured in our model only for larger ϵ, away from onset. Selection near onset can be measured by Fourier analysis only for much larger cells than can currently be studied economically, or for different boundary conditions such as periodic boundaries on all sides. It should also be kept in mind that recent theoretical efforts[32,80] have concentrated on *local* wave-number selection, not the distribution of wave numbers obtained by a Fourier analysis.

Given the field at a particular time during its evolution, $\phi(x,y,\tau)$, we can obtain its two-dimensional Fourier transform, $\phi(k_x,k_y,\tau)$, by two successive complex fast Fourier transforms.[28] If the spatial mesh is uniform with rectangles of sides dx and dy, the x and y wave numbers are bounded by the corresponding Nyquist frequencies, $1/2dx$ and $1/2dy$. It is convenient to plot the wave-number power spectrum, $P(k_x,k_y,\tau)=|\phi(k_x,k_y,\tau)|^2$ over the region $[0,K]\times[0,K]$ where $K=\min(1/2dx, 1/2dy)$. All wave numbers of interest fall inside this region. The power spectrum can then be plotted using bilinear interpolation[52] between grid points in wave-vector space. A qualitative feeling for the pattern evolution in Fourier space is given in Fig. 37. Figure 37(a) does indeed

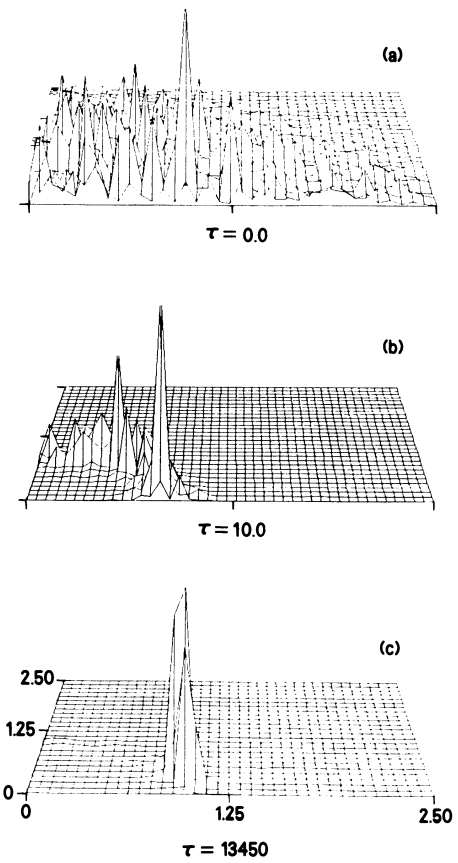

FIG. 37. Wave-number power spectra obtained by spatial Fourier analysis; the values of τ refer to successive stages of evolution in Fig. 10. The random initial conditions in (a) rapidly anneal to a ring of radius close to 1. The large peaks already present in (b) show significant orientation of rolls even at $\tau=10$, and suggest that the fastest growing modes play an important role in pattern formation. (c) reflects the primarily x-oriented rolls in the final state, Fig. 10(f).

show that wave vectors of nearly all length scales occur with random orientation and comparable magnitude. After a short time (10 time units), all short and long wavelengths have annealed out leaving a ring of wave vectors of radius close to 1 [see Fig. 37(b)]. The large peak in the power spectrum on the k_x axis and the second large peak near 45° show that significant orienting of the rolls has already occurred even though the spatial modes still look highly disordered. The stationary state, Fig. 37(c), has nearly all its spectral weight near the k_x axis; the presence of y-oriented cross rolls is barely suggested by the small spectral weight near the k_y axis. We see that pattern formation is especially simple in Fourier space, consisting of the transfer of spectral weight to certain angles along the "critical" arc, $k_x^2+k_y^2=1$. At the same time, the radial width decreases as wave vectors of magnitude slightly larger or smaller than 1 transfer some spectral weight closer to 1.

These results can be stated more quantitatively by calculating the following angular and radial distribution functions:[28]

$$R(\theta)=\int_0^\infty P(K,\theta)KdK\ , \tag{26}$$

$$S(K)=\int_0^{\pi/2} P(K,\theta)Kd\theta\ , \tag{27}$$

where we have rewritten the power spectral density in wave-number polar coordinates ($\theta=0$ and $\theta=\pi/2$ are, respectively, the k_y and k_x axes). From $S(K)$, we can also determine the mean wave number, $\bar{K}$, the linewidth, ΔK, and the skewness of the distribution, s, which are defined by the following:

$$\bar{K}=\int_0^\infty KS(K)dK \Big/ \int_0^\infty S(K)dK\ , \tag{28}$$

$$\Delta K=\left[\int_0^\infty (K-\bar{K})^2 S(K)dK \Big/ \int_0^\infty S(K)dK\right]^{1/2}, \tag{29}$$

$$s=\left[\int_0^\infty (K-\bar{K})^3 S(K)dK \Big/ \int_0^\infty S(K)dK\right] \Big/ \Delta K^3\ . \tag{30}$$

Examples are given in Fig. 38 and Table II. From Fig. 38, we see that the radial distribution, $S(K)$, is not sensitive to the spatial pattern [compare Figs. 15(f) and 16(e)] while $R(\theta)$ in Fig. 38(a) clearly shows the much higher symmetry of Fig. 15(f). The larger density of defects and larger stable band at $\epsilon=0.9$ results in a slightly larger linewidth in Fig. 38(d) compared to Fig. 38(b) (see Table II).

Nearly all the interesting wave-number selection lies in the properties of $S(K)$. Table III gives the widths of the stability band for different ϵ, based on Fig. 31 and its extension to larger ϵ. From Table II, we see that the resolution in linewidth for parallel rolls of the critical wave number is 0.14 for square cells of aspect ratio 16, and 0.08 and 0.12 for x and y rolls in the 20×30 rectangular cell. Thus no wave-number selection can be observed in cells of these sizes close to onset ($\epsilon\lesssim0.1$) for Eq. (1). Cells at least twice as large would be needed for $\epsilon=0.1$. For $\epsilon=0.9$, the final stationary state [Fig. 16(e)] has a distribution, $S(K)$, centered around the critical wave number with a linewidth $\Delta K=0.12$. This is significantly less than the bandwidth of stable wave numbers for $\epsilon=0.9$ given in Table III; wave-number selection has occurred. The results are even more striking for $\epsilon=2.0$. The wave number is close to 1.0 and the width, 0.21, is twice as small as the band of stable wave numbers. Here, the linewidth is also larger than the resolution in linewidth for a cell of this size. The wave-number selection is not complete in the sense that wave numbers beside the critical one survive, probably because of the large density of defects.

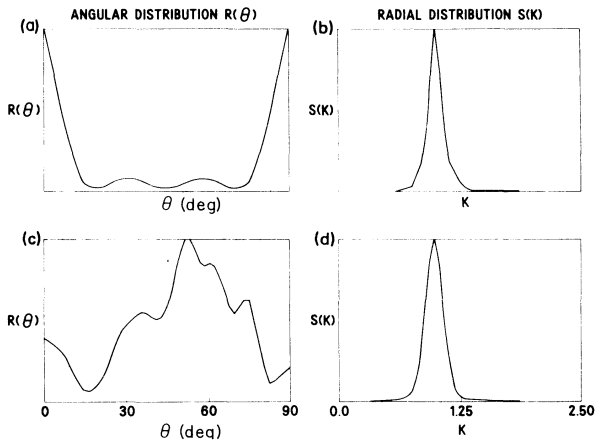

FIG. 38. Angular and radial distribution functions of the wave-number power spectrum calculated for the $\epsilon=0.10$ state of Fig. 15(f) [(a) and (b)] and the $\epsilon=0.90$ state of Fig. 16(e) [(c) and (d)].

From Table II, we see that the mean wave number of the stationary states is always close to the critical wave number, $k_c=1$, with a slight positive skewness, indicating that the wave-number distribution is slanted towards larger wave numbers. The mean wave number is close to 1 for several reasons, e.g., because k_c is the marginally stable wave number,[29] because it is the fast growing mode, or because it minimizes the Lyapunov functional. Figure 37(b) suggests that the growth rate *is* an important factor. The mean wave number of the initial conditions leading to Fig. 37(b) has a value 1.29 and so the mean value *decreases* toward 1 during pattern formation. As defects migrate and annihilate, the average length scale slightly increases. This is in clear contradiction with Gollub's experimental data[28] which show that the mean wave number steadily increases, always remaining significantly less than the critical wave number. One can understand this difference from the low Prandtl number of water, which leads to a marginally stable wave number (to zigzag) which is smaller than the critical wave number near onset.[20] It is less clear how to explain the steady increase of wave numbers with further defect motion, independent of the initial conditions. Truly random initial conditions on all length scales should lead to defects that introduce both larger and smaller wave numbers equally. Why this is not the case experimentally requires further investigation.

TABLE II. Parameters for wave-number power spectrum.

Description of pattern	$\bar{K}$ First moment	ΔK Linewidth	s Skewness
Square cell, $\Gamma=16$, parallel x rolls	1.01	0.14	0.8
Square cell, $\Gamma=16$, $\epsilon=0.90$ [Fig. 16(e)]	1.00	0.12	0.4
Square cell, $\Gamma=16$, $\epsilon=0.10$ [Fig. 15(f)]	1.02	0.12	1.4
Rectangular cell, $\Gamma=20\times30$, parallel y rolls	1.01	0.12	2.3
Rectangular cell, $\Gamma=20\times30$, parallel x rolls [Fig. 9(a)]	1.00	0.08	0.8
Rectangular cell, $\Gamma=20\times30$, Fig. 10 at $\tau=0$	1.29	0.56	0.2
Rectangular cell, $\Gamma=20\times30$, Fig. 10 at $\tau=10$	1.00	0.11	0.7
Rectangular cell, $\Gamma=20\times30$, Fig. 10 at $\tau=13450$	1.01	0.06	1.0
Rectangular cell, $\Gamma=20\times30$, Fig. 18(e)	0.97	0.21	0.3

TABLE III. Width of stability band of Eq. (1) for different ϵ (from Fig. 31).

ϵ	Width ΔK
0.10	0.10
0.90	0.24
2.00	0.40

VIII. CONCLUSIONS AND FUTURE PROSPECTS

In this paper, we have investigated various details of pattern formation in the presence of lateral boundaries and nonlinear terms for a simple two-dimensional relaxational equation. Because this equation is related by perturbation theory to the Boussinesq equations near the onset of convection, we were able to investigate several interesting theoretical issues relevant to real systems. We studied the resolution of spatial degeneracy, the origin of long-time scales, and wave-number selection and related our calculations to a variety of experiments close to onset. Our analysis has been intermediate between analytical theory and experiment in an attempt to bring the two closer together.

There are two essential conclusions. First, our simulations show that there is a two-dimensional scalar equation that can be successfully used to study the three-dimensional dynamics of the five Boussinesq equations close to onset. State-of-the-art numerical techniques were used to simulate and to explore a new regime of large convection cells and long-time scales. We also found that Eqs. (1) and (3) seem to describe the shorter length and time scales correctly, particularly pattern formation in small- and intermediate-aspect-ratio cells.[8,9]

Second, our numerical calculations have illustrated the strong influence of the confining boundaries in determining the stationary pattern and the time scale to achieve this pattern. We have seen, for example, how random initial conditions of complicated defect configurations in large rectangular and square cells evolve to a unique stationary state (close to onset) which reflects in its orientation and texture the size and geometry of the container. The time scale to become stationary, in turn, is much larger in square cells because of the higher symmetry and degeneracy. In the presence of periodic boundaries, all defects eventually disappear near onset. The final state, now attained on the time scale of a horizontal diffusion time or less, consists of parallel or wavy rolls oriented independently of the cell boundaries. The degeneracy is therefore much larger. As the reduced Rayleigh number is increased, the healing length near the boundaries becomes comparable with a roll diameter and the possible disorder of the convection texture increases, barriers to defect gliding appear, and the time for the evolution to become stationary becomes less than a horizontal-diffusion time. We conclude that the presence of rigid boundaries and of two distinct length scales is the source of the long-time scales observed near onset for the pattern to become stationary.

Many details in our simulations remain to be tested experimentally. We find that the most stable stationary patterns near onset are not symmetric and have defects.[8] The degeneracy of these stationary states is surprisingly small, which seems to differ with the observations of Gollub *et al.*[19] For higher Rayleigh numbers, our model predicts[26] that the most stable patterns are symmetric and without defects but are never achieved by random initial conditions because of large barriers to defect motion. Specific stationary states close to onset were calculated (Figs. 6, 7, 9, 10, 15, 19, and 20) and suggest obvious experiments for comparison. The simulations show that the dominant mechanism of pattern formation near onset is the elimination of defects from the interior of the cell and dislocation gliding towards corners or along the shorter sides of rectangular cells. Further optical experiments with controlled initial conditions would be useful to explain how dislocations glide and whether different core structures[21] move differently, especially as a function of Prandtl number. The long-time scales for large-cells' patterns to become stationary suggest that complicated defect motion might involve time scales that are larger than the time scales of the box geometry. Recent arguments by Cross and Newell[80] suggest that this time to become stationary might scale as the *cube* of the lateral dimensions (as opposed to the square of those dimensions, based on a horizontal diffusion time). While our simulations are consistent with this prediction, further numerical and experimental efforts are needed. Finally, we find that, close to *onset, the vertical heat transport (Nusselt number) is in*sensitive to the details of pattern formation, increasing monotonically and smoothly (in the absence of metastable states) towards a stationary value. Both close to and away from onset, the mean-square amplitude was found to be a maximum for the most stable state [which minimizes the Lyapunov functional, Eq. (4)]. This signature provides a straightforward way to determine over what range in Rayleigh number Eqs. (1) and (3a) will be relevant to experiment.

We conclude by suggesting some further analytical and numerical investigations that would be useful. First, the effect of different kinds of cell geometries on pattern formation and wave-number selection could be studied by using cylindrical and annular cells. The case of large cylindrical cells is especially interesting since so little is known about the corresponding spatial pattern formation. Long two-dimensional cells could test the one-dimensional theory that shows how the band of stable wave numbers near onset is severely restricted in the presence of lateral boundaries.[33,34] The reduced Rayleigh number could be made a space- and time-dependent field, $\epsilon(x,y,t)$, to examine the role of periodic[55] or random[56] modulations or stationary spatial gradients.[30] A slow ramping of a homogeneous value, $\epsilon(t)$, would give initial conditions closer to those used in many experiments and show how pattern formation depends on the ramping rate.[59] Different cubic terms in Eq. (1), such as[41] $\nabla[(\nabla\phi)^2\nabla\phi]$, lead to stable square cells of superimposed rolls,[67] a pattern that is predicted to occur in Rayleigh-Bénard convection in the limit of nearly insulating horizontal plates.[81] Using the numerical methods of Sec. III, it would then be straightforward to study the role of lateral boundaries in the evolution of rectangular convection textures.[41,67,82] Perhaps

the most promising future investigation would be the study of rotationally invariant, two-dimensional equations that match the perturbation expansion of the Boussinesq equations to higher order, including the Prandtl-number dependent effects of vertical vorticity[45] and mean drift[46] on roll curvature. Such models have the two important properties of being nonrelaxational and having a skewed-varicose instability.[67] Recent initial explorations[36,82] using the numerical methods and approach of this paper look promising and might help to understand the key remaining mystery of Ahlers and Behringer's experiment,[16] why this simplest and weakest of nonequilibrium systems becomes turbulent close to onset.

ACKNOWLEDGMENTS

We would like to thank G. Ahlers, P. Bjørstad, M. Cross, J. Gollub, P. Hohenberg, W. Petersen, D. Rose, N. Schryer, and R. Walden for many fruitful stimulating conversations and suggestions regarding the physics, experimental data, and numerical methods discussed in this paper.

---

*Present address: Princeton Plasma Physics Laboratory, P. O. Box 451, Princeton, NJ 08544.

[1]S.-k. Ma, *Modern Theory of Critical Phenomena* (Benjamin, Reading, Mass., 1976).

[2]P. C. Martin, J. Phys. (Paris) Colloq. **37**, C1-57 (1976); D. Forster, *Hydrodynamic Fluctuations, Broken Symmetry, and Correlation Functions* (Benjamin, Reading, Mass, 1975); L. Sneddon, Phys. Rev. A **24**, 1629 (1981).

[3]C. Normand, Y. Pomeau, and M. Verlarde, Rev. Mod. Phys. **49**, 581 (1977).

[4]F. H. Busse, Rep. Prog. Phys. **41**, 1929 (1978).

[5]J. P. Gollub, in *Nonlinear Dynamics and Turbulence,* edited by D. Joseph and G. Iooss (Pittman, New York, 1982).

[6]R. Graham, Phys. Rev. A **10**, 1762 (1974).

[7]J. Swift and P. C. Hohenberg, Phys. Rev. A **15**, 319 (1977).

[8]M. C. Cross, Phys. Rev. A **25**, 1065 (1982).

[9]K. Stork and U. Müller, J. Fluid Mech. **54**, 599 (1972).

[10]M. M. Chen and J. A. Whitehead, J. Fluid Mech. **31**, 1 (1968).

[11]H. Oertel, Jr., in *Natural Convection in Enclosures,* edited by K. E. Torrance and I. Catton (American Society of Engineers, New York, 1980).

[12]J.-P. Eckmann, Rev. Mod. Phys. **53**, 643 (1981); M. I. Rabinovich, Usp. Fiz. Nauk **125**, 123 (1978) [Sov. Phys. Usp. **21**, 443 (1979)]; R. May, Nature (London) **261**, 459 (1976).

[13]J. P. Gollub and S. V. Benson, J. Fluid Mech. **100**, 449 (1980).

[14]M. J. Feigenbaum, J. Stat. Phys. **19**, 25 (1978).

[15]D. Rand, S. Ostlund, J. Sethna, and E. D. Siggia, Phys. Rev. Lett. **49**, 132 (1982).

[16]G. Ahlers and R. P. Behringer, Prog. Theor. Phys. Suppl. **64**, 186 (1979).

[17]G. Ahlers and R. W. Walden, Phys. Rev. Lett. **44**, 445 (1980).

[18]R. P. Behringer and G. Ahlers, J. Fluid Mech. **125**, 219 (1982).

[19]J. P. Gollub, A. R. McCarriar, and J. F. Steinman, J. Fluid Mech. **125**, 259 (1982).

[20]F. H. Busse and R. M. Clever, J. Fluid Mech. **91**, 319 (1979).

[21]E. D. Siggia and A. Zippelius, Phys. Rev. A **24**, 1036 (1981).

[22]Y. Pomeau, S. Zaleski, and P. Manneville, Phys. Rev. A **27**, 2710 (1983).

[23]A. C. Newell and J. A. Whitehead, J. Fluid Mech. **38**, 279 (1969).

[24]L. A. Segel, J. Fluid Mech. **38**, 203 (1969).

[25]C. Normand, J. Appl. Math. Phys. **32**, 81 (1981).

[26]H. S. Greenside, W. M. Coughran, Jr., and N. L. Schryer, Phys. Rev. Lett. **49**, 726 (1982).

[27]E. L. Koschmieder, in *Advances in Chemical Physics* **26**, edited by I. Prigogine and S. A. Rice (Wiley, New York, 1974), p. 177.

[28]J. P. Gollub and A. R. McCarriar, Phys. Rev. A **26**, 3470 (1982).

[29]A. Pocheau and V. Croquette, J. Phys. (Paris) **45**, 35 (1984).

[30]L. Kramer, E. Ben-Jacob, H. Brand, and M. Cross, Phys. Rev. Lett. **49**, 1891 (1982).

[31]G. Dee and J. S. Langer, Phys. Rev. Lett. **50**, 383 (1983); D. Aronson and N. Weinberger, Adv. Math. **30**, 33 (1978).

[32]Y. Pomeau and P. Manneville, J. Phys. (Paris) **42**, 1067 (1981).

[33]M. C. Cross, P. G. Daniels, P. C. Hohenberg, and E. D. Siggia, Phys. Rev. Lett. **45**, 898 (1980).

[34]M. C. Cross, P. G. Daniels, P. C. Hohenberg, and E. D. Siggia, J. Fluid Mech. **127**, 155 (1983).

[35]Y. Pomeau and S. Zaleski, J. Phys. (Paris) **42**, 515 (1981).

[36]P. Bjørstad, W. M. Coughran, Jr., H. S. Greenside, D. J. Rose, and N. L. Schryer, in *Elliptic Problem Solvers II,* edited by G. Birkhoff and A. Schoenstadt (Academic, New York, 1984).

[37]J. Wesfreid, Y. Pomeau, M. Dubois, C. Normand, and P. Bergé, J. Phys. (Paris) Lett. **39**, L725 (1978).

[38]M. Cross, Phys. Fluids **23**, 1727 (1980).

[39]A. C. Newell, in *Fourth Symposium on Synergetics,* edited by H. Haken (Springer, New York 1979); F. H. Busse, J. Fluid Mech. **30**, 625 (1967).

[40]G. I. Sivashinsky, Physica (Utrecht) **4D**, 227 (1982).

[41]V. L. Gertsberg and G. I. Sivashinsky, Prog. Theor. Phys. **66**, 1219 (1981).

[42]Y. Kuramoto, Prog. Theor. Phys. Suppl. **64**, 346 (1978).

[43]G. I. Sivashinsky, Annu. Rev. Fluid Mech. **15**, 179 (1983).

[44]M. C. Cross, Phys. Fluids **25**, 936 (1982).

[45]E. D. Siggia and A. Zippelius, Phys. Rev. Lett. **47**, 835 (1981); A. Zippelius and E. D. Siggia, Phys. Fluids **26**, 2905 (1983).

[46]M. C. Cross, Phys. Rev. A **27**, 490 (1983).

[47]J. A. Whitehead, J. Fluid Mech. **75**, 715 (1976).

[48]P. Bjørstad, SIAM J. Numer. Anal. **20**, 59 (1983).

[49]P. Bjørstad (private communication).

[50]P. Manneville, J. Phys. (Paris) **44**, 563 (1983). Manneville used an explicit time-integrating scheme and a crude approximation for the boundary conditions but obtained physically meaningful solutions similar to those described for medium-sized cells in Sec. IV. He also found that simple nonpotential changes of Eq. (1) did not lead to nonperiodic evolution in his cell.

[51]S. A. Orszag, Stud. Appl. Math. **50**, 293 (1971); D. Gottlieb and S. A. Orszag, *Numerical Analysis of Spectral Methods: Theory and Application* (Society for Industrial and Applied Mathematics, Philadelphia, England, 1977).

[52]G. Dahlquist and Å. Björck, *Numerical Methods* (Prentice-Hall, Englewood Cliffs, New Jersey, 1974).
[53]N. L. Schryer, in *Proceedings of the ACM National Meeting, San Diego, 1974,* (ACM, New York, 1974).
[54]R. E. Bank and D. J. Rose, Numer. Math. **37**, 279 (1981).
[55]G. Ahlers, P. Hohenberg, and M. Lücke, Bull. Am. Phys. Soc. **26**, 1271 (1981, and unpublished); J. P. Gollub and S. V. Benson, Phys. Rev. Lett. **41**, 948 (1978).
[56]J. P. Gollub and J. F. Steinman, Phys. Rev. Lett. **45**, 551 (1980).
[57]A new generation of experiments that measure optical and thermal data simultaneously and accurately has started to appear, e.g., R. W. Walden, A. Passner, P. Kolodner, and C. M. Surko, Bull. Am. Phys. Soc. 28, 460 (1983).
[58]We are indebted to M. C. Cross for suggesting the usefulness of this approximation.
[59]G. Ahlers, M. C. Cross, P. C. Hohenberg, and S. Safran, J. Fluid Mech. **110**, 297 (1981).
[60]S. H. Davis, J. Fluid Mech. **30**, 465 (1967).
[61]The boundary conditions, Eq. (3), mathematically require all rolls to be perpendicular immediately near the cell walls. This does not prevent them from bending through large angles further away from the walls.
[62]The authors are indebted to M. C. Cross and P. C. Hohenberg for this observation.
[63]A. Schlüter, D. Lortz, and F. Busse, J. Fluid Mech. **23**, 129 (1965).
[64]J. P. Gollub, S. V. Benson, and J. Steinman, Ann. NY Acad. Sci. **357**, 22 (1980).
[65]S. Zaleski, Y. Pomeau, and A. Pumir, Phys. Rev. A **29**, 366 (1984).
[66]F. H. Busse, J. Fluid Mech. **30**, 625 (1967).
[67]H. S. Greenside and M. C. Cross (unpublished).
[68]A. H. Bobeck, Bell Sys. Tech. J. **46**, 1901 (1967).
[69]R. E. Rosensweig, in *Fourth Symposium on Synergetics,* edited by H. Haken (Springer, New York, 1979); Sci. Am. **247**, 135 (1982).
[70]H. S. Greenside, G. Ahlers, P. C. Hohenberg, and R. W. Walden, Physica (Utrecht) **5D**, 322 (1982).
[71]C. M. Bender and S. A. Orszag, *Advanced Mathematical Methods for Scientists and Engineers* (McGraw-Hill, New York, 1978).
[72]H. Frick, F. H. Busse, and R. M. Clever, J. Fluid Mech. **127**, 141 (1983).
[73]R. M. Clever and F. H. Busse, J. Fluid Mech. **65**, 625 (1974).
[74]N. W. Ashcroft and N. D. Mermin, *Solid State Physics* (Holt, Rinehart, and Winston, New York, 1976).
[75]F. H. Busse, J. Math Phys. **46**, 140 (1967).
[76]F. H. Busse and J. A. Whitehead, J. Fluid Mech. **47**, 305 (1971).
[77]If the reduced Rayleigh number is suddenly decreased below the critical value ϵ_c the amplitude but not the phase of a stationary solution decays nearly exponentially. Until this amplitude decreases in magnitude below the experimental noise level, there is an effective memory of the system for the previous stationary solution.
[78]A. C. Newell, C. G. Lange, and P. J. Aucoin, J. Fluid Mech. **40**, 513 (1970).
[79]The zig-zag instability and cross-roll cannot occur in a one-dimensional system which greatly simplifies the analysis of Ref. 78.
[80]M. C. Cross and A. Newell, Physica D (Utrecht) (to be published).
[81]F. H. Busse and N. Riahi, J. Fluid Mech. **96**, 243 (1980).
[82]H. S. Greenside and W. M. Coughran, Jr. (unpublished).